

Accepted Manuscript

Dual colour emitting Eu doped strontium orthosilicate phosphors synthesized by bio-template assisted ultrasound for solid state lightning and display applications

M. Venkataravanappa, H. Nagabhushana, B. Daruka Prasad, G.P. Darshan, R.B. Basavaraj, G.R. Vijayakumar

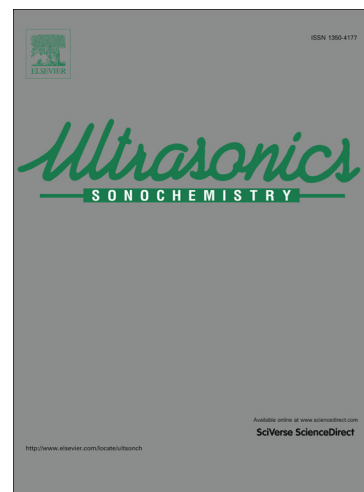
PII: S1350-4177(16)30245-0
DOI: <http://dx.doi.org/10.1016/j.ultsonch.2016.07.004>
Reference: ULTSON 3302

To appear in: *Ultrasonics Sonochemistry*

Received Date: 3 April 2016
Revised Date: 12 June 2016
Accepted Date: 11 July 2016

Please cite this article as: M. Venkataravanappa, H. Nagabhushana, B. Daruka Prasad, G.P. Darshan, R.B. Basavaraj, G.R. Vijayakumar, Dual colour emitting Eu doped strontium orthosilicate phosphors synthesized by bio-template assisted ultrasound for solid state lightning and display applications, *Ultrasonics Sonochemistry* (2016), doi: <http://dx.doi.org/10.1016/j.ultsonch.2016.07.004>

This is a PDF file of an unedited manuscript that has been accepted for publication. As a service to our customers we are providing this early version of the manuscript. The manuscript will undergo copyediting, typesetting, and review of the resulting proof before it is published in its final form. Please note that during the production process errors may be discovered which could affect the content, and all legal disclaimers that apply to the journal pertain.



Dual colour emitting Eu doped strontium orthosilicate phosphors synthesized by bio-template assisted ultrasound for solid state lighting and display applications

M. Venkataravanappa^{1,2}, H. Nagabhushana^{3,*}, B. Daruka Prasad⁴, G.P. Darshan^{5,2},
R.B. Basavaraj³, G.R. Vijayakumar⁶

¹Department of Physics, Govt. First Grade College, Sira, Tumkur 572 103, India

²Research and Development Center, Bharathiar University, Coimbatore 641 046, India

³Prof. C.N.R. Rao Centre for Advanced Materials, Tumkur University, Tumkur 572 103, India

⁴Department of Physics, BMS Institute of Technology, VTU-affiliated, Bangalore 560 064, India

⁵Department of Physics, Acharya Institute of Graduate Studies, Bangalore 560 107, India

⁶Department of Chemistry, University College of Science, Tumkur 572103, India

Abstract

A novel Sr₂SiO₄: Eu (1 – 5 mol %) superstructures (SS) were synthesized using bio-sacrificial *A. V. gel* assisted ultrasound method. Powder X-ray diffraction patterns confirmed the presence of both α and β phase formation. It was evident that morphological growth was highly reliant on *A. V. gel* concentration, sonication time, pH and sonication power. The formation mechanisms for different hierarchical SS were proposed. From diffuse reflectance spectra, the energy band gap was estimated and found to be ~ 4.70 – 5.11 eV. The photoluminescence emission spectra for the excitation at 392 nm, shows characteristic emission peaks at 593, 613, 654 and 702 nm which were attributed to ⁵D₀ → ⁷F₀, ⁷F₁, ⁷F₂ and ⁷F₃ transitions of Eu³⁺ ions respectively. Conversely, when the samples were subjected to the heat treatment at 850 °C for 3 h under argon atmosphere, display an intense broad emission peak with two de-convoluted peaks at 490 and 550 nm due to 4f⁶5d¹ → 4f¹ (⁸S_{7/2}) transitions of Eu²⁺ ion. The concentration quenching phenomenon was discussed which attributes to energy transfer, electron–phonon coupling and ion–ion interaction. The *Judd-Ofelt* intensity parameters and other radiative properties were estimated by using emission spectra. The CIE chromaticity coordinate values of Sr₂SiO₄:Eu²⁺ and Eu³⁺ nanophosphor were located in green and red regions respectively. The calculated CCT and CRI values specify that the present phosphor can be fairly useful for both green and red components of white LED's. Luminescence decay and quantum yield suggest the suitability of this phosphor as an efficient luminescent medium for light emitting diodes. Overall, the results elucidated a rapid, environmentally benign, cost-effective and convenient method for Sr₂SiO₄: Eu synthesis and for the possible applications such as solid state lighting and display devices.

Keywords: Ultrasound; nanophosphor; Light Emitting Diodes; Photoluminescence, SS.

* Corresponding author: +91- 9945954010, E-mail: bhushanvlc@gmail.com (H. Nagabhushana).

1. Introduction

Hierarchical superstructures (SS) were generally composed of a basic building blocks which repeats in a well-defined manner. Hierarchical SS reported until now used capping agents, surfactant molecules, growth promoters / inhibitors, bio-templates in chemical route and vapor phase growth or electro deposition in physical route of synthesis [1]. However, such procedures require either high temperatures or a suitable substrate and hence show very little versatility or flexibility for tuning the underlying architecture.

Recently, silicate based phosphors due to stable crystal structure, high thermal stability, low thermal conductivity, resistance to acids and alkali they were being used in light industry [2]. Among the various silicates, strontium orthosilicate (Sr_2SiO_4) showed applications in the fields of sensors, field emission displays (FEDs), compact fluorescent lamps (CFLs), white light emitting diodes (WLEDs), and plasma display panels (PDPs), etc. It was well known that the luminescent properties of inorganic nano/micro materials were closely related with their sizes, shapes, morphologies, compositions and crystallinity [3]. $\text{Sr}_2\text{SiO}_4:\text{Eu}^{2+}$ absorbs ultraviolet radiation and emits green light when activated by Eu^{2+} ions, however, $\text{Sr}_2\text{SiO}_4:\text{Eu}^{3+}$ phosphors show intense emission in the red region. It was expected that the two fold behavior of $\text{Sr}_2\text{SiO}_4:\text{Eu}^{3+}/\text{Eu}^{2+}$ phosphors might play a positive role in practical applications [4].

Among the various rare earth elements, europium was special as a dopant which shows valence fluctuation property (divalent or trivalent). The red emission of Eu^{3+} was centered at near 612 nm attributes to intra-4f transitions whereas the emission of Eu^{2+} varies in a wide range from red to ultraviolet due to the dipole allowed $5d-4f$ transitions [5].

Till date numerous chemical and physical synthesis routes namely, solution combustion, sol-gel, solid state etc. [6 - 9] were used to prepare silicate nanostructures. Conventionally multi

constituent ceramics have been prepared by solid-state method which involves physical mixing of hydroxides, oxides, carbonates, nitrates and/or sulphate raw materials followed by high temperature treatment, ($> 1500\text{ }^{\circ}\text{C}$) for several hours to get the required phosphor material. The drawback of this method was that the powders obtained in this method were with coarse grained, agglomerated with very low surface area structures. On the other side poor sintering results, inhomogeneous microstructure, abnormal grain growth, lack of control of cation stoichiometry and creation of surface defects which were harmful to luminescence. Further, high temperature sintering resulted in dense and hard phosphors which were difficult to be crushed or grind. Table.1 displays the Sr_2SiO_4 phosphor prepared by diverse routes, formation temperature and their obtained various morphologies [10-16].

In order to obtain nano/micro structured materials at reasonably low temperature was highly essential for industrial applications. Various chemical methods have been proposed and developed over the last few decades. Even though many techniques have been established for the fabrication of nano/micro particles, problems of agglomeration remain a limiting factor for their applications in many fields.

The ultrasound aided route has been widely used to harvest novel phosphors with scarce properties and accepted to be effective for preparing wide range of nano/bulk structured phosphors, including oxides / sulphates / aluminates / fluorides etc. in a short period. The physical and chemical effects generated during ultrasonic irradiation can influence the properties of doped materials. Further, ultrasound assisted synthesis route has great commercial advantages with high production rates, flexibility in synthesis on choosing host materials, high purity nanoparticles, rapid reaction rate, narrow size distributions, stable colloidal dispersion of nanomaterials, uniform mixing, less synthesis time and less energy usage [17]. The ultrasound

effects arise from acoustic cavitation, which results in the formation, growth and implosive collapse of bubbles in a liquid. The growth of the bubble happens through the diffusion of solute vapor into the volume of the bubble, while the collapse of the bubble arises when the bubble size reaches its maximum value. When solution was exposed to ultrasound irradiation, the bubbles were collapsed by acoustic fields in the solution. According to hot spot theory, very high temperatures (> 5000 K) were achieved upon the collapse of a bubble. Since this collapse occurs in less than a nanosecond, very high cooling rates ($> 10^{10}$ K/s) was also obtained. These extreme environments can drive several chemical reactions and physical modifications occur. This helps to tune the particles size distribution, shape and size of the phosphors effectively [18].

In this paper, hierarchical SS of Sr_2SiO_4 : Eu phosphor was prepared using bio-sacrificial *A.V. gel* assisted ultrasound method. *A.V.* is a juicy plant contains nearly 80 potentially active constituents such as polysaccharides, enzymes, minerals, amino acids, alkaloids and flavones etc. These phytochemicals acts as a bio-template which helps in obtaining complex SS in the nano/micro level which improves the light emitting capacity than the prepared samples in the conventional route. The major phytochemicals extracted in *A.V. gel* was confirmed from *GCMS* and shown in Table 2 [19].

To the best of our knowledge, no reports are available on the synthesis of europium doped strontium silicate using bio template assisted ultrasound-sonication method. Herein, for the first time, *A.V.* bio template assisted ultra-sound method to prepare Eu doped Sr_2SiO_4 phosphor reported. In addition, several unique self-oriented SS were also obtained by changing the experimental conditions. Influence on the morphology by sonochemical time, power and the pH of the precursor solution were discussed in detail. The probable formation mechanisms of different hierarchical SS were proposed on the basis of time-dependent experiments. Further, the

luminescent properties of Eu^{3+} (or Eu^{2+}) doped Sr_2SiO_4 phosphors were studied carefully. To evaluate the potential applications of the phosphor CIE, CCT and CRI of Sr_2SiO_4 : Eu nano/microstructures were studied.

2. Materials and Methods

2.1 Extraction of A. V. gel

Preparation of the A. V. gel (A.V), A.V. leaves were collected from the plants grown in the garden of the Department of Physics, Tumkur University, Tumkur, India (Latitude: 13.34° N and Longitude : 77.11° E). Leaves were washed thoroughly with double distilled water to remove the dust particles. The detailed procedure for the collection of A.V. plant gel was described elsewhere [20].

2.2 Synthesis

Stoichiometric quantities of strontium nitrate and tetraethyl orthosilicate were dissolved in the distilled water and thoroughly mixed in a magnetic stirrer to get uniform solution. The stoichiometric amount of europium nitrate (1- 5 mol %) was added to above resulting solution. Further, A.V. extract was added to the resultant mixture slowly. Then the mixture was stirred ultrasonically (ultrasonic frequency ~ 20 kHz, power ~ 150 W) at a fixed temperature of 75°C for various ultrasonic time (1 - 6 h). The solution was kept undisturbed until a white precipitate was formed along with polymeric networks of protein and polysaccharide complex chains in which the nanoparticles trapped. The precipitate was filtered and washed several times by using distilled water and ethanol to remove any unreacted material. The obtained product was dried at 60°C for 3 h in a vacuum oven. Further the product was divided into two parts for characterization (i) calcined at 600°C for 3 h in air atmosphere (ii) calcined at 850°C for 3 h

under argon atmosphere. The schematic representation for the synthesis of Eu doped Sr_2SiO_4 nanophosphor was shown in Fig.1.

2.2. Characterization

Phase purity and crystallinity of nanophosphors were measured using a powder X-ray diffractometer (XRD, Shimadzu 7000). $\text{CuK}\alpha$ (1.541 Å) radiation with nickel filter was used to obtain diffraction data and a flat-bed sample holder in a transmission mode. The patterns were recorded with a 130° image plate detector at room temperature (RT) and at ambient pressure. Scanning electron microscopy (SEM) measurements were performed on a Hitachi table top, Model TM 3000. The prepared samples were dispersed on a sticky carbon pad. Transmission electron microscopy (TEM) was performed on a Hitachi H-8100 accelerating voltage up to 200 KV, LaB_6 filament equipped with EDS (Kevex sigma TM Quasar, USA). To get better image quality, the thin layer of Ag was deposited on the sample which was dispersed on a copper grid. The diffuse reflectance of the samples was recorded on Perkin Elmer (35- λ) spectrometer. The Jobin Yvon Spectrofluorimeter Fluorolog-3 with 450 W Xenon lamp as an excitation source was used for photoluminescence (PL) measurements.

3. Results and discussion

Fig. 2 (a) shows the power X-ray diffraction (PXRD) patterns of synthesized Eu^{3+} (or Eu^{2+}) doped Sr_2SiO_4 phosphors. The PXRD patterns of Eu^{3+} (or Eu^{2+}) doped Sr_2SiO_4 confirmed to be the monoclinic β -phase when $x \leq 3$ mol %. Further, when $x = 4$ mol %, the spectra exhibit dual (both β & α) phase. The β -phase (monoclinic with space group:P21/n-14) transfers to the α -phase (orthorhombic with space group:Pnma-62) when $x = 5$ mol %. The PXRD patterns of β and α phase were well matched with JPCDS 38-0271 and JPCDS 39-1256 respectively [21]. The PXRD patterns indicates that the doped Eu^{3+} (or Eu^{2+}) ions successfully substituted in the host

lattices. The host Sr_2SiO_4 displays iso-structure nature, where Sr^{2+} ions have two different cation sites in the lattice: Sr (I) and Sr (II) sites. The cationic Sr (I) and Sr (II) sites were coordinated by ten O^{2-} ions forms a chain along c-axis and nine O^{2-} ions forms a chain along b-axis respectively with one side of Si^{4+} ions. In general, the Sr (II) sites were more asymmetric than that of Sr (I). Therefore, Eu^{3+} (or Eu^{2+}) ions may occupy two different sites of Sr (I) and Sr (II) [4].

The acceptable percentage difference (D_r) between radii of dopant Eu^{3+} ions (0.947 Å) and substituted Sr^{2+} ions (1.31 Å) was found to be 27 % as explained in the literature [22].

The average crystallite size (D) was calculated by using Scherrer's formula [23],

$$D = \frac{0.89\lambda}{\beta \cos \theta} \quad \text{----- (1)}$$

where D ; the average crystallite size, λ ; the wavelength of the X-rays (0.15406 nm), and θ ; the diffraction angle and β ; full-width at half maximum (FWHM) of the peaks in the PXRD patterns. The 'D' values were calculated for $\text{Sr}_2\text{SiO}_4:\text{Eu}^{3+}$ (1 – 5 mol %) nanophosphors and listed in Table.3. It was observed from the table that the variation in the crystallite size depends on the dopant Eu^{3+} concentration. This was due to the increased strain which leads to the replacement of Sr^{2+} ions by Eu^{3+} ions. To calculate the crystallite size and strain present in the nano/microstructures, W–H (Williamson–Hall) fitting method was used [24]. The strain can be estimated by taking the slope of the linear fit between $(\beta \cos \theta / \lambda)$ along y-axis and $(4 \sin \theta / \lambda)$ along x-axis as shown in Fig.3. The estimated values of size and strain were summarized in a Table.3.

The diffused reflectance spectra (DRS) of $\text{Sr}_2\text{SiO}_4:\text{Eu}^{3+}$ (1-5 mol %) nanophosphor was shown in Fig.4 which displays a strong band in the shorter wavelength region (< 250 nm) was ascribed due to absorption of the host lattice. The several sharp weak bands were observed due to

meta- stable energy states formed between the valence band and conduction band by the Eu^{3+} ions. These electronic bands were the characteristics of Eu^{3+} ions, starting from ground state ${}^7\text{F}_0$ to the various excited states of Eu^{3+} ions [25].

The optical energy band gap of $\text{Sr}_2\text{SiO}_4:\text{Eu}^{3+}$ nanophosphors were determined by Kubelka–Munk (K-M) function using DRS. The intercept of the tangents to the plots of $[F(R_\infty)h\nu]^{1/2}$ versus photon energy $h\nu$ was shown in Fig. 5. The Kubelka–Munk function $F(R_\infty)$ and photon energy ($h\nu$) were estimated by following relations[26]:

$$F(R_\infty) = \frac{(1 - R_\infty)^2}{2R_\infty} \quad \text{----- (2)}$$

$$h\nu = \frac{1240}{\lambda} \quad \text{----- (3)}$$

where R_∞ ; reflection coefficient of the sample, λ ; the absorption wavelength. The calculated band gap energies were listed in Table.3. The degree of structural order and disorder into the matrix was leads to changes in E_g and also which will change the distribution of energy levels within in the band gap [27]. Furthermore, the degree of structural order–disorder of the matrix was mainly depends on the preparation methods as well as experimental conditions which can favor or slow down the formation of structural defects, which was also cause for the variation in the E_g . Here a blue shift was observed in the E_g value with the increase in the dopants concentration.

Microstructural analysis

It was well known that when compared to conventional routes; optimized sonication parameters generally results in lesser particle sizes, uniform particle size distribution and reduced synthesis time. When the ultrasonic frequency of 20 kHz was applied, shorter nano plates undergo self-assembly to form micro flower and the tip of petal start folding outwards (Fig.6 (a)). When there is an increase in the ultrasonic frequency to 22 kHz, the surface of micro flowers become

smoother due to well assembly of nano plates and further folding of petals can be observed (Fig.6 (b)). However, when the ultrasonic frequency was further increased to 24 kHz and 26 kHz, petals of the micro flowers will grow further and becomes fully folded outwards. SEM images of $\text{Sr}_2\text{SiO}_4:\text{Eu}^{3+}$ (2 mol %) nanophosphor with sonication power 22 kHz with its enlarged portions was shown in Fig.7.

Surfactant with an appropriate concentration can be an auxiliary component in obtaining various self-assembled nano/micro structures [28]. The effect of various concentrations of A.V. gel (5 - 20 ml) on morphology was investigated with fixed sonication time (1 h) and was shown in Fig.8. For 5 ml A.V. gel concentration, long hexagonal cone shaped particles to form a stack of dried tropical banana leaf patterns (Fig.8 (a)). This was due to the fact that A.V. gel acts as a “capping agent” to bound on some specific facets and provide the preferred growth direction to nanocrystals. When the concentration of A.V. gel was increased exactly two fold, (10 ml) the concentration of an individual cone shaped particles with large pores spread out in different directions (Fig.8 (b)). At higher A.V. concentration (15 ml), the pores at the tips were short and small dendritic growth was observed (Fig.8 (c)). However, further increase of A.V. gel concentration to 20 ml, no cone shaped particles were noticed (Fig.8 (d)). This was due to the fact that less adsorption of A.V. molecules would be favorable for the growth of Sr_2SiO_4 crystals, possibly due to the weaker stabilizing effect of the surfactant. Association of Sr^{2+} with the anionic head group can reduce the repulsive force between surfactant head groups. The schematic representation for the formation process of SS in $\text{Sr}_2\text{SiO}_4:\text{Eu}$ phosphor with different concentration of A.V. gel was shown in Fig.9.

To the best of our knowledge and through review of literature, such well-defined hexagonal long cone shaped particles have not reported for Sr_2SiO_4 so far. It is well known that

when two particles of dissimilar sizes collides each other, there will be an affinity for ions to dissolve from the surface of the smaller particle and precipitate on the surface of the larger one due to the transmission of electrons. Consequently, the particles with bigger sizes will grow at the expense of the smaller ones. The continuous irreversible process of hitting and sticking, mainly along the preferred growth direction, initiates the primary growth of combs. This large, new and random superstructure signifies several forms of growth, in which one after other particles was formed and then diffuses, sticks to the growing structure. The incessant oriented hitting, sticking and subsequent Oswald ripening shows a similar growth behavior to “Oriented attachment”, which was observed in a system where small particles selectively adsorb the surfactant molecules and allow them to join together with complete crystallographic alignment and restrict the degrees of freedom.

In the reaction mixture, surfactant molecules (*A.V.*), which normally act as a molecularly dissolved surface modifier or stabilizer, may be a kind of capping agent which was chemically absorbed onto the surface of nanoparticles which will kinetically controls the growth rate through adsorption and desorption. However, the macroscopic morphology influenced by microscopic effects was not very clear up to now and needs further investigation. Thus, the bio-surfactant-template method offers a route to control the Sr_2SiO_4 : Eu morphology over a much wider range than previously reported techniques by simply changing the concentration of additives as well as *A.V.* gel.

Fig.10. shows the SEM images for Sr_2SiO_4 SS which were synthesized by ultrasonication with different time both in the absence and presence of *A.V.* gel extract. It was evident that non-uniform structures were obtained in the absence of *A.V.* gel, however in the presence of it a different types of SS was obtained. The plausible mechanism for the formation of Sr_2SiO_4 SS

was given in Fig.11. In the beginning free radicals $H\cdot$ and $OH\cdot$ were obtained by ultrasonication [29] which further reacts with TEOS to form orthosilicic acid (H_4SiO_4). Further H_4SiO_4 reacts with strontium nitrate to form strontium orthosilicate. Thus the obtained particles were reoriented in the presence of organic constituents present in the A.V. gel to form various SS. A.V. gel contains major constituents such as tetracontane (29.8%), Guanosine (19%), 1-phenyl ethanone (13%) and Pentadecanoic acid (6.8%) were confirmed by gas chromatograph mass spectrometer (GCMS) [19]. Among these constituents, tetracontane possess non-polar chain group and rest of the compounds contains both polar and non-polar heads. All these molecules acts as surfactant which helped in obtaining self-assembled SS under certain conditions. It is believed that, in aqueous medium and in the absence of Sr_2SiO_4 particles, primary aggregation of these molecules could takes place to form micelles structures with non-polar chains of interior and polar heads becomes exterior. With the increase in sonication time, polar heads of the organic molecules will interact with the primarily particles of Sr_2SiO_4 NPs and new structures were formed (Fig.11). The polar group of organic molecules was attached to Sr^{2+} through physical union which further facilitates the typical crystallization and rearrangement of the Sr_2SiO_4 NPs. Finally with the increase in sonication time the perfect self-orientation takes place along with uniform SS were resulted.

A.V. gel comprises several multifunctional organic compounds and active ingredients extracted using GCMS and the major components along with chemical structures was given in Table.2. When strontium nitrate mixed with A.V. gel, the Sr^{2+} ions will locate regularly, thus establishing a three-dimensional polymeric network structure. The resultant polymeric networks experience slow breakdown when subjected to ultrasound treatment. Further, the creation of

polymer network controls the rate of reaction; as a result well-ordered uniform Sr_2SiO_4 SS were obtained.

Morphological features were studied under different pH conditions (Fig.12). It was evident from SEM images that pH value may significantly affect the morphology of the product. Moreover by varying the suitable pH value of the precursor solution, size and dimension of the assembly units significantly alter [30]. In the growth stage, many of the small assembly units spread out divergently to form hierarchical SS and at this stage surface energy was reduced. The definite creation processes was more complex and may need more conformational studies. Several factors may influence to acquire hierarchical SS, including crystal- face attraction, electrostatic and dipolar fields associated with the aggregate, Vander Waals forces, intrinsic structures and external factors. The schematic representation of possible growth mechanisms to end up with various hierarchical SS was shown in Fig.13.

TEM, HRTEM images, and SAED patterns were as shown in Fig.14 corresponds to Sr_2SiO_4 : Eu^{3+} (1, 3 & 5 mol %) and Sr_2SiO_4 : Eu^{2+} (1, 3 & 5 mol %) compounds obtained with 1 h sonication time respectively. The TEM images shows thin sheet like nano structures of Sr_2SiO_4 prepared using 1, 3 and 5 mol % Eu. The high resolution TEM image shows the well-defined crystal planes with an average spacing of ~ 0.23 nm, ~ 0.32 nm, and ~ 0.30 nm respectively for the above-mentioned three compositions Sr_2SiO_4 : Eu^{3+} (1, 3 & 5). The SAED patterns were well matched with the (hkl) values corresponding to the prominent peaks of the PXRD profiles.

Photoluminescence (PL) Properties

Inset of Fig. 15 shows the PL excitation spectrum of Sr_2SiO_4 : Eu^{2+} (2 mol %) nanophosphor recorded at 548 nm emission. The spectrum exhibits a broad peak at 380 nm due to transition from ground state $4f^7$ to the excited state $4f^65d^1$ of Eu^{2+} ions. The broad band excitation band

at ~ 390 – 650 nm indicates that present phosphor was a promising material for WLEDs [4]. The PL emission spectra of $\text{Sr}_2\text{SiO}_4:\text{Eu}^{2+}$ (1 - 5 mol %) nanophosphor excited at 380 nm was shown in Fig.15. Single emission peak recorded at 490 nm (Eu_1) and 550 nm (Eu_2) which was ascribed to transition of $4f^65d^1 \rightarrow 4f^7$ ($^8\text{S}_{7/2}$) of Eu^{2+} ions which involve 5d orbitals [31]. This effect is due to the crystal field and it shows the stabilization of Eu^{2+} at two different sites. It is in agreement with the earlier reports. PL decay corresponding to these emissions were due to Eu^{2+} situated at SrO_{10} sites and Sr_9 sites respectively, exhibits mono-exponential behaviour with lifetime values of 5.46 and 5.98 ms. The asymmetric band signifies that Eu^{2+} ions occupy more than one site in the Sr_2SiO_4 lattice sites [32]. The emission occurs in terms of the parity-allowed transition from the excited state to the ground state. The strong crystal field strength has a splitting effect on the 5d orbit by lowering its energy level. So the energy level of the Eu^{2+} in two different sites experiences different splitting effect and thus the energy levels were different. Such phenomenon also explains that the two Eu^{2+} emissions occur at two cation sites [33].

The excitation spectrum of Eu^{3+} doped Sr_2SiO_4 (2 mol %) nanophosphor was recorded under 613 nm emission (inset Fig.16). The spectrum contains of three different regions; (i) $f-f$ transitions, (ii) Charge transfer transition and (iii) Band to band absorption.

The spectra exhibit sharp peaks at ~ 321, 360, 380, 392, 414 and 463 nm were attributed to transition of $^7\text{F}_0 \rightarrow ^5\text{F}_3, ^5\text{H}_6, ^7\text{D}_4, ^5\text{L}_7, ^5\text{L}_6, ^5\text{D}_3$ and $^5\text{D}_2$ respectively [34].

The position of charge transfer band was estimated by Jorgensen formula [35];

$$E_{ct} (\text{cm}^{-1}) = [\chi_{opt}(X) - \chi_{opt}(M)] 30 \times 10^3 \text{ cm}^{-1} \quad \text{----- (4)}$$

where $\chi_{opt}(X)$ and $\chi_{opt}(M)$; optical electronegativities of the ligand and central metal ion respectively, E_{ct} ; the energy of charge transfer band. Substituting the values of $\chi_{opt}(X) = 0.95$ and $\chi_{opt}(M)(\text{Eu}^{3+}) = 1.78$ into Eq. (4), the position of $\text{O}^2 \rightarrow \text{Eu}^{3+}$ CTB can be

calculated to be ~ 401 nm. Excitation spectrum also contains the absorption band at ~ 401 nm of $\text{Sr}_2\text{SiO}_4:\text{Eu}^{3+}$ which corresponds to host absorption in $\text{Sr}_2\text{SiO}_4:\text{Eu}^{3+}$.

The emission from inorganic phosphors originates from the complex interaction among the host matrix, activators, defects, sensitizers and interfaces. Luminescence of the trivalent europium ions results from the intra $4f-4f$ electron transitions. Since the 4f electrons are well shielded from the surrounding environment by the external electric fields of the outer closed 5s and 5p electrons, characteristic narrow line like emissions are produced. Fig. 16 shows the PL emission spectra of $\text{Sr}_2\text{SiO}_4:\text{Eu}^{3+}$ (1 – 5 mol %) nanophosphor excited at 392 nm. The spectra exhibits characteristic emission peaks at 593, 613, 654 and 702 nm which were due to ${}^5\text{D}_0 \rightarrow {}^7\text{F}_0$, ${}^5\text{D}_0 \rightarrow {}^7\text{F}_1$, ${}^5\text{D}_0 \rightarrow {}^7\text{F}_2$, and ${}^5\text{D}_0 \rightarrow {}^7\text{F}_3$ $4f^6$ configuration of Eu^{3+} ions, respectively. The intense peak at 613 nm was due to transition ${}^5\text{D}_0 \rightarrow {}^7\text{F}_2$ and was hyper sensitive aroused due to a forced electric dipole transition mechanism. The other peak at 593 nm was due to magnetic dipole transition of ${}^5\text{D}_0 \rightarrow {}^7\text{F}_1$ and was insensitive to site symmetry [36, 37]. Energy levels diagram of Eu^{3+} and Eu^{2+} doped Sr_2SiO_4 nanophosphor was shown in Fig.17.

The crystal field asymmetry of Sr_2SiO_4 around the Eu^{3+} ions can be determined by evaluating the hypersensitive asymmetric ratio (A) [38]. It can also provide an estimate of the covalent nature and polarization of the nearby Eu^{3+} ions by short range effects. Greater the asymmetric ratio, more distortion from inversion symmetry which was calculated as the ratio of the integrated emission intensity of electric (${}^5\text{D}_0 \rightarrow {}^7\text{F}_2$) to magnetic (${}^5\text{D}_0 \rightarrow {}^7\text{F}_1$) dipole transitions as

$$A_{21} = \frac{\int I_2({}^5\text{D}_0 \rightarrow {}^7\text{F}_2) d\lambda}{\int I_1({}^5\text{D}_0 \rightarrow {}^7\text{F}_1) d\lambda} \quad \text{----- (5)}$$

where I_1 and I_2 ; intensity of magnetic dipole transition at 593 nm and electric dipole transition at 613 nm respectively. This ratio depends on the cation site occupancies, bond lengths, bond angles, distortion of the lattice and nature of host matrix. Therefore the value of A_{21} for $\text{Sr}_2\text{SiO}_4:\text{Eu}^{3+}$ decreases with the increase in Eu^{3+} concentration (Fig. 18). The variation of asymmetric ratio with doping concentration can influence the luminescent property of a material and also used to determine the optimum concentration of rare-earth in the host for luminescence applications.

The effect of doping concentration (Eu^{3+} and Eu^{2+}) on the emission intensity of the host was shown in Fig.19. The PL intensity increased with increase of concentration of Eu^{3+} and Eu^{2+} up to 2 mol % and afterwards it diminishes. The decrease in PL intensity was due to phenomena known as self-concentration quenching [35]. The phenomena of self- concentration quenching was due to: (i) Defect to $\text{Eu}^{3+}/\text{Eu}^{2+}$ energy transfer, (ii) multiphonon assisted energy transfer by electron – phonon coupling and (iii) $\text{Eu}^{3+}-\text{Eu}^{3+}$ energy transfer. In the present case, energy transfer between defect to $\text{Eu}^{3+}/\text{Eu}^{2+}$ was not observed, this indicates that this type of energy transfer was not responsible for concentration quenching in the present studies. In the excitation spectrum of $\text{Sr}_2\text{SiO}_4:\text{Eu}^{3+}$ nanophosphor, transition ${}^7\text{F}_0 \rightarrow {}^5\text{D}_2$ was a pure electric dipole (PED) transition, therefore, weak bands located between 380 - 450 nm due to transitions ${}^7\text{F}_0 \rightarrow {}^5\text{D}_2$ and ${}^7\text{F}_0 \rightarrow {}^5\text{D}_3$ can correspond to phonon assisted transitions (PAT) and was shown in Fig.20. PED can be ascribed by one or multi-phonon processes. Thus it is clear from the energy levels of Eu^{3+} that energy difference between ${}^5\text{D}_2$ and ${}^5\text{D}_3$ (2500 cm^{-1}) was much larger than vibrational energies of chemical bonds in inorganic compounds [39]. In multi-phonon process, the non-radiative rate W_{NR} can be calculated by using the modified exponential energy-gap equation of Van Dijk and Schuurmans

$$W_{NR} = \beta_{el} \exp[-\alpha(\Delta E - 2\hbar\omega_{\max})] \quad \text{----- (6)}$$

where β_{el} (10^7 s^{-1}) and α ($4.5 \times 10^{-3} \text{ cm}$); constants respectively and $\hbar\omega_{\max}$; the energy of the active phonons. The estimated multiphonon relaxation was found to be 254 s^{-1} which was relatively small and cannot responsible for concentration quenching for RE ion doped materials [40]. Huang–Rhys factor S was used to characterize the phonon-assisted transition (PAT) for determine non-radiative transition given by the relation [41];

$$S = \frac{I_{PAT}}{I_{ZP}} \quad \text{----- (7)}$$

where I_{PAT} and I_{ZP} ; the integrated intensities of the phonon-assisted transition and zero phonon line, respectively. The calculated Huang–Rhys factor S was found to be 0.33, which was greater than reported value. The value of the Huang–Rhys factor proves the existence of week electron-phonon coupling between Eu^{3+} dopant and Sr_2SiO_4 host. Thus multiphonon assisted energy transfer was not responsible for cause of quenching.

Hence it may be concluded that the non-radiative energy transfer between the rare earth $\text{Eu}^{3+}/\text{Eu}^{2+}$ ions was reason for concentration quenching. The non-radiative energy transfer between $\text{Eu}^{3+}/\text{Eu}^{2+}$ was mainly due to the exchange interaction, radiation reabsorption or a multipole–multipole interaction. The self-quenching of $\text{Eu}^{3+}/\text{Eu}^{2+}$ ions can happen when the separation between the two closest Eu^{3+} ions was such that the interaction between the two $\text{Eu}^{3+}/\text{Eu}^{2+}$ ions was conceivable which leads to increase in the non-radiative relaxation and diminish the luminescence intensity. Initially, the PL intensity increases and then decreases due to smaller radius of $\text{Eu}^{3+}/\text{Eu}^{2+}$ as compared to Sr^{2+} ions but at higher intensity the charge imbalance leads to cross relaxation and on radiative transitions causes concentration quenching [42]. At higher

concentration of $\text{Eu}^{3+}/\text{Eu}^{2+}$ ions the distance between the activator ions decreases which leads to the non-radioactive energy transfer among Eu^{3+} ions.

To know type of interaction mechanism, critical distance (R_c) between the neighboring $\text{Eu}^{3+}/\text{Eu}^{2+}$ ions can estimated by using Blasse formula [43]:

$$R_c \approx 2 \left(\frac{3V}{4\pi X_c N} \right)^{\frac{1}{3}} \quad \text{----- (8)}$$

where V ; the volume of the unit cell, X_c ; the critical concentration $\text{Eu}^{3+}/\text{Eu}^{2+}$ ions and N ; the number of sites in the unit cell. Presently, V ; 391.2 \AA^3 , X_c ; about 0.02 and N ; 4, resulting in the critical distance of $\sim 8.3 \text{ \AA}$. The estimated R_c value was greater than 5 \AA for the $\text{Eu}^{3+}/\text{Eu}^{2+}$ ions leads to the multipole–multipole interaction in the Sr_2SiO_4 host and was the major reason for concentration quenching of $\text{Eu}^{3+}/\text{Eu}^{2+}$ ions in host. The schematic representation for concentration quenching phenomena was shown in Fig.21. Suppose electric multipolar interaction was responsible in the energy transfer, there were several types of interactions may be possible namely dipole–dipole (d–d), dipole–quadrupole (d–q), quadrupole–quadrupole (q–q), etc. Therefore it was necessary to reveal which type of interaction is responsible in the energy transfer. According to Dexter and Schulman, emission intensity (I) per activator ion can be expressed by the following equation [44]:

$$\frac{I}{\chi} = K \left[1 + \beta (\chi)^{\frac{Q}{3}} \right]^{-1} \quad \text{----- (9)}$$

Where χ ; the activator concentration, Q ; a constant of multi- polar interaction and equals 6, 8, or 10 and less than 6 for dipole–dipole; dipole– quadrupole or quadrupole–quadrupole interactions and charge transfer mechanism respectively, and K and β ; constants for the given host lattice under the same excitation condition.

$$\text{Log } \frac{I}{\chi} = A - \frac{Q}{3} \log \chi \quad \text{----- (10)}$$

where ($A = \log k - \log \beta$). The curve of $\log I/\chi$ v/s. $\log \chi$ in $\text{Sr}_2\text{SiO}_4: \text{Eu}^{3+} / \text{Eu}^{2+}$ phosphor was shown in Fig. 22 and clearly confirms that the relation was approximately linear and the value of slope for Eu^{3+} and Eu^{2+} was ~ 1.964 and 1.938 respectively. The calculated value Q for Eu^{3+} and Eu^{2+} was found to be 5.892 and 5.814 respectively and were almost equal to 6 . This result indicates that the charge transfer mechanism was due to d-d interaction for the concentration quenching transition of $\text{Sr}_2\text{SiO}_4: \text{Eu}^{3+} / \text{Eu}^{2+}$ phosphor.

Judd–Ofelt analysis

Detailed investigation on the site symmetry and luminescence dynamics of Eu^{3+} ion in Sr_2SiO_4 was evaluated by analyzing the Judd–Ofelt intensity parameters. Judd-Ofelt analysis was a powerful spectroscopic technique, which effectively describes the spectral behavior in a specific coordination environment of rare earth ions doped single and polycrystalline materials, glasses and solutions. Through this analysis one can determine the rates of parity forbidden electric dipole transitions between different electronic levels of the rare earth ion, understand the local structural environment around the rare earth ion and can evaluate the bond covalency of rare earth and its associated ligands [45, 46]. The relation between radiative emission rates and the integrated emission intensities was given by the equation [47]:

$$\frac{A_{0-2,4}}{A_{0-1}} = \frac{I_{0-2,4}}{I_{0-1}} = \frac{h\nu_{0-1}}{h\nu_{0-2,4}} \quad \text{----- (11)}$$

where I_{0-J} and $h\nu_{0-J}$; integrated emission intensity and energies corresponding to transition ${}^5\text{D}_0 \rightarrow {}^7\text{F}_J$ ($J=1, 2, 4$) respectively.

The radiative transition rates (A_{0-J}) of electric dipole is expressed as

$$A_{(0-J)} = \frac{64\pi^4 \nu_J^3}{3h(2J+1)} \frac{n(n^2+2)^2}{9} \sum_{J=2,4} \Omega_J \left| \left\langle {}^5D_0 \parallel U^{(J)} \parallel {}^7F_J \right\rangle \right|^2 \text{-----} (12)$$

where $A_{(0-J)}$; the coefficient of spontaneous emission, e ; the electronic charge, ν_J ; the wavenumber of the corresponding transition, h ; the Planck's constant and n ; the refractive index of the prepared sample. $\left| \left\langle {}^5D_0 \parallel U^{(J)} \parallel {}^7F_J \right\rangle \right|^2$; squared reduced matrix element of Eu^{3+} and were 0.0032 and 0.0023 for $J = 2$ and 4 respectively and these values were independent of the chemical environment [48], $J=6$ was neglected due to very small number. Thus, by using Eqs. (11) and (12), the values of Ω_2 and Ω_4 were calculate and tabulated in Table.4. The variation in the value of Ω_2 with different Eu^{3+} concentration specifies that Ω_2 was more sensitive to the ligand environment. This means that Ω_2 parameter value was attributed to the covalency and structural changes in the vicinity of the Eu^{3+} ion exhibiting short range effect whereas the Ω_4 parameter was dependent on the viscosity and dielectric constant of the host causing long range effect. For $\text{Sr}_2\text{SiO}_4: \text{Eu}^{3+}$ nanophosphor, the Ω_2 value was increased with the increase of Eu^{3+} concentration up to 3 mol %, which indicates stronger covalence of Eu-O bonding and lower symmetry around the Eu^{3+} ion. Smaller values of Ω_4 obtained for $\text{Sr}_2\text{SiO}_4: \text{Eu}^{3+}$ shows appreciable rigidity of the crystalline host matrix. The Ω_6 intensity parameter could not be calculated here because ${}^5D_0 \rightarrow {}^7F_3$ emission was quite weak and was not observed in the present case.

The radiative properties such as transition probabilities (A_T), radiative lifetimes (τ_{rad}) and branching ratios (β_R) for the excited states of Eu^{3+} ion were calculated by using estimated value of J-O parameters with following equations [49].

$$A_T(\psi J) = \sum_{J'} A_{J-J'} \quad \text{----- (13)}$$

$$\tau_{rad}(\psi J) = \frac{1}{A_T(\psi J)} \quad \text{----- (14)}$$

$$\beta(\psi J) = \frac{A(\psi J, \psi' J')}{A_T(\psi J)} \quad \text{----- (15)}$$

The measured branching ratio (β) for Eu^{3+} - doped Sr_2SiO_4 nanophosphor to be $\beta \geq 0.50$ suggests that present nanophosphor can emit laser radiation more effectively and was suitable for red color displaying devices respectively.

Colour characteristics

The colour perception corresponding to luminescence of Eu^{3+} and Eu^{2+} dopant ions in the Sr_2SiO_4 host was studied. Colour perception is a physicophysical property of the human eye and this response was expressed by mathematically in terms of CIE coordinates given by the Commission Internationale de L'Eclairage for illumination. In general, the emission colour of any phosphor can be represented by the (x, y) chromaticity coordinates [50, 51]. The CIE coordinates were estimated using PL emission spectra and the values were listed in a Table.5. The CIE chromaticity diagram corresponding to of $\text{Sr}_2\text{SiO}_4: \text{Eu}^{3+}/\text{Eu}^{2+}$ with different concentrations were shown in Fig.23. It was noticed that the CIE co-ordinates for $\text{Sr}_2\text{SiO}_4: \text{Eu}^{3+}$ (x = 0.6181, y = 0.3814) for 2 mol % was located in red region and nearly same as the National Television System Committee (NTSC) standard values of pure red color (0.67, 0.33). By varying the concentration of Eu^{3+} ions from 1 to 5 mol %, color tuning can be achieved. However in the case of $\text{Sr}_2\text{SiO}_4: \text{Eu}^{2+}$, CIE co-ordinates were located in the green region.

The correlated color temperature (CCT) was one the important parameter to know the color appearance of the light emitted by a source, relating its color with respect to a reference light source when heated up to a specific temperature, in Kelvin (K) [52]. The CCT was calculated by transforming the (x, y) coordinates of the light source to (U_0, V_0) by using the relations by determining the temperature of the closest point of the Planckian locus to the light source on the (U', V') uniform chromaticity diagram (Fig.24) [53]:

$$U' = \frac{4x}{-2x+12y+3} \text{----- (16)}$$

$$V' = \frac{9y}{-2x+12y+3} \text{----- (17)}$$

Further, the quality of white light was checked in terms of color correlated temperature (CCT) was given by McCamy empirical formula $CCT = -437 n^3 + 3601 n^2 - 6861 n + 5514 .31$ (theoretical) where $n = (x - x_c)/(y - y_c)$; the inverse slope line and chromaticity epicenter was at $x_c = 0.3320$ and $y_c = 0.1858$ [54]. The CCT values estimated for both $\text{Sr}_2\text{SiO}_4: \text{Eu}^{3+}$ and Eu^{2+} (1 - 5 mol %) nanophosphor was summarized in Table.5 and the obtained values were well acceptable range and quite useful in home appliances. The effect of Eu^{3+} and Eu^{2+} on the colour purity of phosphor was also analyzed using the relation [55];

$$\text{color purity} = \frac{\sqrt{(x_s - x_i)^2 + (y_s - y_i)^2}}{\sqrt{(x_d - x_i)^2 + (y_d - y_i)^2}} \times 100\% \text{----- (18)}$$

where (x_s, y_s) ; the coordinates of a sample point, (x_d, y_d) ; the coordinates of the dominant wavelength and (x_i, y_i) ; the coordinates of the illuminant point. The estimated values were

given in Table.5, which specified that purity of the red color enhances with increase of Eu^{3+} concentration.

Life time measurements and Quantum yield:

To understand the behaviour of luminescence decay, the optimized decay data (2 mol % of Eu-ions) was fitted with various decay equations [56]. It was found that curves follow two types of exponential decays for Eu^{2+} and Eu^{3+} doped Sr_2SiO_4 .

$$I(t) = I_1 e^{-\frac{t}{\tau_1}} + I_2 e^{-\frac{t}{\tau_2}} \quad \text{.....(19)}$$

Similarly for tri-exponential decay

$$I(t) = I_1 e^{-\frac{t}{\tau_1}} + I_2 e^{-\frac{t}{\tau_2}} + I_3 e^{-\frac{t}{\tau_3}} \quad \text{.....(20)}$$

$$\tau_{avg} = \frac{I_1 \tau_1^2 + I_2 \tau_2^2}{I_1 \tau_1 + I_2 \tau_2} \quad \text{.....(21)}$$

And

$$\tau_{avg} = \frac{I_1 \tau_1^2 + I_2 \tau_2^2 + I_3 \tau_3^2}{I_1 \tau_1 + I_2 \tau_2 + I_3 \tau_3} \quad \text{.....(22)}$$

The corresponding average life time values were estimated using the equations (21) and (22) respectively and found to be 5.54 ms and 5.19 ms for bi-exponential and tri-exponential fitted data. The variation in exponential decay fit may be due to the

- 1) Difference in the non-radiative probability of decays for Eu-ions at or near the surface and ions embedded inside the material.
- 2) Heterogeneous distribution of the doping ions in the host material leads to the change in local concentration. and
- 3) The transfer of excitation energy from donor to Eu activators.

Quantum efficiency (QE) was of two types, external QE also called as quantum yield (η) and internal QE. External QE was related to number of photons incident on the sample and number of photons emitted whereas the internal QE was related to the radiative transition and non-radiative energy transfer relaxation which are responsible for the depopulation of multiplet. The values of external QE for the 2 mol % $\text{Sr}_2\text{SiO}_4:\text{Eu}^{2+}$ and $\text{Sr}_2\text{SiO}_4:\text{Eu}^{3+}$ were found to be 4.45 % and 7.35% respectively. Whereas estimated internal QE for the 2 mol % $\text{Sr}_2\text{SiO}_4:\text{Eu}^{2+}$ and $\text{Sr}_2\text{SiO}_4:\text{Eu}^{3+}$ were found to be 82.32 % and 77.11 % respectively. The estimated values of external QE were very less compared to internal QE. This is due to the small values of extraction coefficient for the materials based on the effective refractive indices values estimated from Sellemer's equation [57].

4. Conclusions

In summary, 3D micro flowers with definite textured morphologies have been successfully prepared via a facile, bio-sacrificial *A.V. gel* assisted ultrasound method and a subsequent low temperature calcination treatment. Additionally, the shape, size and structures of the products can be controlled well by changing the reaction parameters. By ultrasonic irradiation, growth of stable nano crystalline $\text{Sr}_2\text{SiO}_4:\text{Eu}^{3+}/\text{Eu}^{2+}$ SS were fabricated at RT, under the action of bio-sacrificial *A.V. gel* as surfactant/capping agent. Similarly, use of ultrasonic irradiation instead of conventional mechanical stirring provides significant advantages including improved crystallinity, reduced particle-size and larger surface area of SS (bulk / nano) in a short time. Thus, this synergistic route of bio surfactant mediated ultrasound synthesis of Sr_2SiO_4 offers a simple, direct, cost effective and eco-friendly method of synthesis, applicable on large industrial scale. In this process, the bio-template plays an important role in the formation of various morphologies. In Sr_2SiO_4 host, $\text{Eu}^{3+}/\text{Eu}^{2+}$ ions have two different cation sites in the lattice: Sr (I)

and Sr (II) sites. Therefore, Eu^{3+} (or Eu^{2+}) ions often occupy at different sites, which encourages different luminescent properties. The PXRD patterns revealed that the phosphors were composed of orthorhombic $\alpha\text{-Sr}_2\text{SiO}_4$ and monoclinic $\beta\text{-Sr}_2\text{SiO}_4$ phase. By altering the charge state of $\text{Eu}^{(+3/+2)}$, the color of the phosphor can be varied. The CIE co-ordinates ($x = 0.6181$, $y = 0.3814$) for $\text{Sr}_2\text{SiO}_4:\text{Eu}^{3+}$ (2 mol %) was located in pure red region which is nearly same as the National Television System Committee (NTSC) standard values of pure red color. By varying the concentration of Eu^{3+} ions from 1 to 5 mol %, color tuning can be observed. The CIE co-ordinates for $\text{Sr}_2\text{SiO}_4:\text{Eu}^{2+}$ was located in the green region. The above results clearly indicate that the phosphor fabricated in ultrasound route can be highly useful for display and solid state lighting applications.

Acknowledgement

The author Dr. H Nagabhushana thanks to DST Nano Mission, New Delhi for the sanction of this project.

ACCEPTED MANUSCRIPT

References:

- [1]. V. Pachauri, K. Kern, K. Balasubramanian, Template-free self-assembly of hierarchical ZnO structures from nanoscale building blocks, *Chem. Phys. Lett.*, 498 (2010) 317-322
- [2]. I. P. Sahu, D. P. Bisen, N. Brahme, Impulsive excitation of mechanoluminescence in europium activated strontium orthosilicate phosphor, *J Mater Sci: Mater Electron* 27 (2016) 3934–3940.
- [3]. Q. Yanmin, Z. Xinbo, Y. Xiao, C. Yan, G. Hai, Photoluminescent properties of $\text{Sr}_2\text{SiO}_4:\text{Eu}^{3+}$ and $\text{Sr}_2\text{SiO}_4:\text{Eu}^{2+}$ phosphors prepared by solid-state reaction method, *J. Rare Earths*, 27, (2009), 323-326.
- [4]. F. Wei, Q. Jia, Massive production of $\text{A}_2\text{SiO}_4:\text{Eu}^{3+}$ and $\text{A}_2\text{SiO}_4:\text{Eu}^{2+}$ (A = Ca, Sr, Ba) microspheres and luminescent properties, *Superlattices Microstruct.* 82 (2015) 11–17.
- [5]. M. Jayasimhadri, E. Cho, J. Jeong, H.S. Lee, K. Jang, S.S. Yia, J.H. Jeong, Luminescence properties of Eu^{2+} doped $\text{Sr}_2\text{SiO}_4\text{-Mg}_2(\text{Si}_2\text{O}_6)$ mixed phases for white-light emitting diodes, *Optoelectron Adv. Mat.*, 3 (2009) 415 – 417.
- [6]. H. Nagabhushana, B. M. Nagabhushana, M. M. Kumar, C. H. Rayappa, K. V. R. Murthy, C. Shivakumara, R. P. S. Chakradhar, Synthesis, characterization and photoluminescence properties of $\text{CaSiO}_3:\text{Eu}^{3+}$ red phosphor, *Spectrochim Acta Part A* 78 (2011) 64-69.
- [7]. D. V. Sunitha, H. Nagabhushana, S. Ch. Sharma, B. M. Nagabhushana, R. P. S. Chakradhar, *J. Alloys Compd.* 575 (2013) 434-443.
- [8]. R. B. Basavaraj, H. Nagabhushana, B. Daruka Prasad, S. C. Sharma, S. C. Prashantha, B. M. Nagabhushana, A single host white light emitting $\text{Zn}_2\text{SiO}_4:\text{Eu}^{3+}$ (Eu, Dy, Sm) Phosphor for LED applications, *Optik*, 12 (2015) 1745-1756.
- [9]. H. Nagabhushana, D. V. Sunitha, S. C. Sharma, B. Daruka Prasad, B. M. Nagabhushana, R. P. S. Chakradhar, Enhanced luminescence by monovalent alkali metal ions in $\text{Sr}_2\text{SiO}_4:\text{Eu}^{3+}$ nanophosphor prepared by low temperature solution combustion method, *J. Alloys Compd.* 595 (2014) 192-199.
- [10]. Z. Pan, H. He, R. Fu, S. Agathopoulos, X. Song, Influence of Ba^{2+} -doping on structural and luminescence properties of $\text{Sr}_2\text{SiO}_4:\text{Eu}^{2+}$ phosphors, *J. Lumin.* 129 (2009) 1105–1108.
- [11]. S.K. Gupta, M. Mohapatra, S. Kaity, V. Natarajan, S.V. Godbole, Structure and site selective luminescence of sol-gel derived $\text{Eu}^{3+}:\text{Sr}_2\text{SiO}_4$, *J. Lumin.* 132 (2012) 1329–1338.
- [12]. J. H. Park, W. Ahn, Y. J. Kim, Phase formation and luminescence of $\text{Sr}_2\text{SiO}_4:\text{Eu}^{3+}$ nanopowders prepared by a hybrid process, *Ceram. Int.* 41 (2015) 734–739.
- [13]. H. Feng, Y. Yang, X. Zhang, Y. Xu, J. Guan, Synthesis and luminescence of $\text{Sr}_2\text{SiO}_4:\text{Eu}^{3+}$ micro-spherical phosphors by a spray-drying process, *Superlattices Microstruct.* 78 (2015) 150–155.
- [14]. R.Y. Yang, H. Y. Chen, S. J. Chang, Y. K. Yang, Effect of Eu^{3+} concentration on microstructure and photoluminescence of $\text{Sr}_2\text{SiO}_4:\text{Eu}^{3+}$ phosphors prepared by microwave assisted sintering, *J. Lumin.* 132 (2012) 780–783.
- [15]. J. Y. Tang, H. Zhong, L. Y. Hao, X. Xu, Synthesis of the uniform hollow spherical $\text{Sr}_2\text{SiO}_4:\text{Eu}^{2+}$ phosphors via an h-BN protective method, *Opt. Mater.* 35 (2013) 2618–2623.

- [16]. H. Y. Chen, R. Y. Yang, S. J. Chang, Y. K. Yang, Microstructure and photoluminescent properties of $\text{Sr}_2\text{SiO}_4:\text{Eu}^{3+}$ phosphors with various NH_4Cl flux concentrations, *Mater Res. Bull.*, 47 (2012) 1412–1416.
- [17]. A. Tavakoli, M. Sohrabi, A. Kargari, A Review of Methods for Synthesis of Nanostructured Metals with Emphasis on Iron Compounds, *Chem. Pap.* 61 (2007) 151-170.
- [18]. R. Ashiri, Obtaining a novel crystalline/amorphous core/shell structure in barium titanate nanocrystals by an innovative one-step approach, *RSC Adv.*, 5 (2015) 48281-48289.
- [19]. K. Alia, S. Dwivedi, A. Azam, Q. Saquib, M. S. Al-Said, A. A. Alkhedhairi, J. Musarrat, A.V. extract functionalized zinc oxide nanoparticles as nanoantibiotics against multi-drug resistant clinical bacterial isolates, *J. Coll. Inter. Sci.* 472 (2016) 145-156.
- [20]. V. K. Patel, S. Bhattacharya, High-performance nanothermite composites based on aloevera directed CuO nanorods. *ACS Appl. Mater. Interfaces*, 5 (2013)13364–13374.
- [21]. Q. Yanmin, Z. Xinbo, Y. Xiao, C. Yan, G. Hai, Photo-luminescent properties of $\text{Sr}_2\text{SiO}_4:\text{Eu}^{3+}$ and $\text{Sr}_2\text{SiO}_4:\text{Eu}^{2+}$ phosphors prepared by solid-state reaction method, *J. Rare Earths*, 27 (2009) 323-326.
- [22]. G.P. Darshan, H.B. Premkumar, H. Nagabhushana, S.C. Sharma, S.C. Prashanth, B. Daruka Prasad, Effective fingerprint recognition technique using doped yttrium aluminate nano phosphor material, *J. Coll. Inter. Sci.* 464 (2016) 206-218.
- [23]. G. Ramakrishna, Ramachandra Naik, H. Nagabhushana, R.B. Basavaraj, S.C. Prashantha, S.C. Sharma, K.S. Anantharaju, White light emission and energy transfer ($\text{Dy}^{3+} \rightarrow \text{Eu}^{3+}$) in combustion synthesized YSO: Dy^{3+} , Eu^{3+} nanophosphors, *Optik*, 127 (2016) 2939-2945.
- [24]. H. Nagabhushana, R.B. Basavaraj, B. Daruka Prasad, S.C. Sharma, H.B. Premkumar, Udayabhanu, G.R. Vijayakumar, “Facile EGCG assisted green synthesis of raspberry shaped CdO nanoparticles”, *J. Alloys Compd.*, 669 (2016) 232-239. X. Zhang, M. Chen, J. Zhang, X. Qin, M. Gong, Photoluminescence studies of high-efficient red-emitting $\text{K}_2\text{Y}(\text{WO}_4)(\text{PO}_4):\text{Eu}^{3+}$ phosphor for NUV LED, *Mater. Res. Bull.* 73 (2016) 219–225.
- [25]. A. E. Morales, E. S. Mora, U. Pal, Use of diffuse reflectance spectroscopy for optical characterization of un-supported nanostructures, *Rev. Mex. Fis.* 53 (2007) 18-22.
- [26]. J.B. Prasannakumar, Y.S. Vidya, K.S. Anantharaju, G. Ramgopal, H. Nagabhushana, S.C. Sharma, B. Daruka Prasad, S.C. Prashantha, R.B. Basavaraj, H. Rajanaik, K. Lingaraju, K.R. Prabhakara, H.P. Nagaswarupa, Bio-mediated route for the synthesis of shape tunable $\text{Y}_2\text{O}_3:\text{Tb}^{3+}$ nanoparticles: Photoluminescence and antibacterial properties, *Spectrochim Acta Part A*, 151 (2015) 131-140.
- [27]. Alpana A. Thorat, Sameer V. Dalvi, Particle formation pathways and polymorphism of curcumin induced by ultrasound and additives during liquid antisolvent precipitation, *Cryst. Eng. Comm.*, 16 (2014) 11102- 11114.
- [28]. C. Gong, D. P. Hart, Ultrasound Induced Cavitation and Sonochemical Yields, *J. Acoust. Soc. America*, 104 (1998).
- [29]. M. Venkataravanappa, H. Nagabhushana, G.P. Darshan, B. Daruka Prasad, G.R. Vijayakumar, H. B Premkumar, Udayabhanu, Novel EGCG assisted ultrasound synthesis of self-assembled $\text{Ca}_2\text{SiO}_4:\text{Eu}^{3+}$ hierarchical SS: Photometric characteristics and LED applications, *Ultrason. Sonochem.* 33 (2016) 226-239.

- [30]. G. Annadurai, S. Masilla Moses Kennedy, V. Sivakumar, Luminescence properties of a novel green emitting $\text{Ba}_2\text{CaZn}_2\text{Si}_6\text{O}_{17}:\text{Eu}^{2+}$ phosphor for white light - emitting diodes applications, *Superlattices Microstruct.* 93 (2016) 57-66.
- [31]. S. K. Gupta, S. Nigam, A. K. Yadav, M. Mohapatra, S. N. Jha, C. Majumder, D. Bhattacharyya, An insight into local environment of lanthanide ions in $\text{Sr}_2\text{SiO}_4:\text{Ln}$ (Ln = Sm, Eu and Dy), *New J. Chem.* 39 (2015) 6531-6539.
- [32]. H. He, R. Fu, X. Song, D. Wang, J. Chen. White light-emitting $\text{Mg}_{0.1}\text{Sr}_{1.9}\text{SiO}_4:\text{Eu}^{2+}$ phosphors. *J. Lumin.* 128 (2008) 489-493.
- [33]. X. Zhang, M. Chen, J. Zhang, X. Qin, M. Gong, Photoluminescence studies of high-efficient red-emitting $\text{K}_2\text{Y}(\text{WO}_4)(\text{PO}_4):\text{Eu}^{3+}$ phosphor for NUV LED, *Mater. Res. Bull.* 73 (2016) 219–225.
- [34]. M. Chowdhury, S. K. Sharma, Spectroscopic behavior of Eu^{3+} in SnO_2 for tunable red emission in solid state lighting devices, *RSC Adv.*, 5 (2015) 51102-51109.
- [35]. S. Som, A. K. Kunti, Vinod Kumar, Vijay Kumar, S. Dutta, M. Chowdhury, S. K. Sharma, J. J. Terblans, H. C. Swart, Defect correlated fluorescent quenching and electron phonon coupling in the spectral transition of Eu^{3+} in CaTiO_3 for red emission in display application *J. Appl. Phys.* 115(2014) 193101-193114.
- [36]. L. Mengting, J. Baoxiang, Synthesis and photoluminescence properties of $\text{ZnTiO}_3:\text{Eu}^{3+}$ red phosphors via sol-gel method, *J. Rare Earths.* 33 (2015) 231-238.
- [37]. M. Chandrasekhar, H. Nagabhushana, S.C. Sharma, K.H. Sudheer kumar, N. Dhananjaya, D.V. Sunitha, C. Shivakumara, B.M. Nagabhushana, Particle size, morphology and color tunable $\text{ZnO}:\text{Eu}^{3+}$ nanophosphors via plant latex mediated green combustion synthesis, *J. Alloys Compd.* 584 (2014) 417– 424.
- [38]. J. M. F. Van Dijk and M. F. H. Schuurmans, On the nonradiative and radiative decay rates and a modified exponential energy gap law for $4f-4f$ transitions in rare-earth ions, *J. Chem. Phys.* 78 (1983) 5317-5323.
- [39]. V. Kumar, S. Som, S. Dutta, S. Das, H. C. Swart, Red-light-emitting inorganic $\text{La}_2\text{CaZnO}_5$ frameworks with high photoluminescence quantum efficiency: Theoretical approach, *Mater Des.*, 93 (2016) 203-215.
- [40]. S. Dutta, S. Som, S. K. Sharma, Luminescence and photometric characterization of K+ compensated $\text{CaMoO}_4:\text{Dy}^{3+}$ nanophosphors, *Dalton Trans.*, (2013) 9654-9664.
- [41]. G. Blasse, Energy transfer between inequivalent Eu^{2+} ions, *J. Solid State Chem.* 62 (1986) 207-211.
- [42]. G. Blasse and B. C. Grabmarier, *Luminescent Materials* (Springer-Verlag, Berlin, 1994), 99.
- [43]. D. L. Dexter and J. H. Schulman, Theory of concentration quenching in inorganic phosphors, *J. Chem. Phys.* 22 (1954) 1063–1070.
- [44]. B. R. Judd, Optical absorption intensities of rare-earth ions, *Phys Rev.* 127 (1962) 750.
- [45]. G S Ofelt, Intensities of crystal spectra of rare-earth ions, *J. Chem. Phys.* 37 (1962) 37, 511-520.
- [46]. J. Feng, H. Zhang, Hybrid materials based on lanthanide organic complexes: a review *Chem. Soc. Rev.* 42 (2013) 387-410.
- [47]. C. A. Kodaira, H. F. Brito, O. L. Malta, Luminescence and energy transfer of the europium (III) tungstate obtained via the Pechini method, *J. Lumin.* 101 (2003) 11–21.
- [48]. S. Som, S. Das, S. Dutta, H. G. Visser, M. K. Pandey, P. Kumar, R. K. Dubey, S. K. Sharma, Synthesis of strong red emitting $\text{Y}_2\text{O}_3:\text{Eu}^{3+}$ phosphor by potential chemical routes:

- comparative investigations on the structural evolutions, photometric properties and Judd–Ofelt analysis, *RSC Adv.* 5 (2015) 70887-70898.
- [49]. Publication CIE no 17.4 (1987) International Lighting Vocabulary, Central Bureau of the Commission Internationale de L'Eclairage, Vienna, Austria.
- [50]. Publication CIE no 15.2 (1986) Colorimetry, Second Edition, Central Bureau of the Commission Internationale de L'Eclairage, Vienna, Austria.
- [51]. János Schanda, M Danyi, Correlated Color-Temperature Calculations in the CIE 1976 Chromaticity Diagram, *Color Res. Appl.* 2 (1977) 161-163.
- [52]. K.M. Girish, Ramachandra Naik, S.C. Prashantha, H. Nagabhushana, H. P Nagaswarupa, K.S. Anatha Raju, H.B. Premakumar, S.C. Sharma, B. M. Nagabhushana, $\text{Zn}_2\text{TiO}_4:\text{Eu}^{3+}$ nanophosphor: Self explosive route and its near UV excited photoluminescence properties for WLEDs, *Spectrochim. Acta Part A*, 138 (2015) 857-865.
- [53]. C.S. McCamy, Correlated color temperature as an explicit function of chromaticity coordinates, *Color Res. Appl.* 17 (1992) 142-144.
- [54]. X. Xu, Y. Tang, F. Mo, L. Zhoun, B. Li, Synthesis and luminescent properties of $\text{CaTiO}_3:\text{Eu}^{3+}$, Al^{3+} phosphors, *Ceram. Int.* 40(2014)10887–10892.
- [55]. S. Dutta, S. Som, S. K. Sharma, Excitation spectra and luminescence decay analysis, *RSC Adv.*, 5 (2015) 7380.
- [56]. W. D. A. M. de Boer, C. McGonigle, T. Gregorkiewicz, Y. Fujiwara, S. Tanabe and P. Stallinga, *Sci. Rep.*, 2014, 4, 5235.

Table Captions:

Table 1: List of $\text{Sr}_2\text{SiO}_4:\text{Eu}^{3+}$ synthesized by different methods, formation temperature and different morphologies of phosphor.

Table 2: List of major phytochemicals extracted in *A. V.* gel confirmed from GCMS.

Table 3: Estimated crystallite size, strain and energy gap (E_g) values of $\text{Sr}_2\text{SiO}_4:\text{Eu}^{3+}$ (1-5 mol %) nanophosphor.

Table 4: Judd-Ofelt intensity parameters (Ω_2 , Ω_4), Emission peak wavelengths (λ_p in nm), radiative transition probability (A_T), calculated radiative (τ_{rad}) lifetime, branching ratio (β_R) and asymmetric ratio (A_{21}) of $\text{Sr}_2\text{SiO}_4:\text{Eu}^{3+}$ (1-5 mol%) compounds ($\lambda_{\text{ex}} = 392$ nm).

Table.5. Photometric characteristics of Eu^{3+} and Eu^{2+} doped Sr_2SiO_4 nanophosphors.

Figure Captions

- Fig.1. Schematic for the synthesis of Eu^{3+} doped Sr_2SiO_4 nanophosphor by ultra-sonication method.
- Fig.2 (a). PXRD patterns of $\text{Sr}_2\text{SiO}_4: \text{Eu}^{3+}$ (1–5 mol %) nanophosphor.
- Fig.2 (b). PXRD patterns of $\text{Sr}_2\text{SiO}_4: \text{Eu}^{2+}$ (1–5 mol %) nanophosphor.
- Fig.3. W–H plots of $\text{Sr}_2\text{SiO}_4: \text{Eu}^{3+}/\text{Eu}^{2+}$ (1–5 mol %) nanophosphor.
- Fig.4. Diffuse reflectance spectra of $\text{Sr}_2\text{SiO}_4: \text{Eu}^{3+}/\text{Eu}^{2+}$ (1–5 mol %) nanophosphor.
- Fig.5. Energy band gaps of $\text{Sr}_2\text{SiO}_4: \text{Eu}^{3+}/\text{Eu}^{2+}$ (1–5 mol %) nanophosphor.
- Fig.6. SEM images of $\text{Sr}_2\text{SiO}_4: \text{Eu}^{3+}$ (2 mol %) nanophosphor with different sonication power (20, 22, 24 and 26 kHz).
- Fig.7. SEM images of $\text{Sr}_2\text{SiO}_4: \text{Eu}^{3+}$ (2 mol %) nanophosphor with sonication power 22 kHz with its enlarged portions.
- Fig.8. SEM images of $\text{Sr}_2\text{SiO}_4: \text{Eu}^{3+}$ (2 mol %) nanophosphor with different concentration of A.V. (5, 10, 15 and 20 ml) with 1hr of ultrasonic irradiation time.
- Fig.9. Schematic representation of formation process of SS in $\text{Sr}_2\text{SiO}_4: \text{Eu}^{3+}$ (2 mol %) nanophosphor with different concentration of A.V..
- Fig.10. Schematic representation of formation process of different SS in $\text{Sr}_2\text{SiO}_4: \text{Eu}^{3+}$ (2 mol %) nanophosphor.
- Fig.11. Schematic representation of $\text{Sr}_2\text{SiO}_4: \text{Eu}^{3+}$ nanostructures in the presence of A.V..
- Fig.12. SEM images of $\text{Sr}_2\text{SiO}_4: \text{Eu}^{3+}$ (2 mol %) nanophosphor with various pH values (5, 7, 9, 11 and 12) with 1hr of ultrasonic irradiation time.
- Fig.13. Schematic representation for the formation of hierarchical SS of $\text{Sr}_2\text{SiO}_4: \text{Eu}^{3+}$ (2 mol %) nanophosphor with various pH values.
- Fig.14. TEM and HRTEM images of $\text{Sr}_2\text{SiO}_4: \text{Eu}^{3+}/\text{Eu}^{2+}$ (1, 3 & 5 mol %) nanophosphor with 1h sonication time.
- Fig.15. (A) PL emission spectra of $\text{Sr}_2\text{SiO}_4: \text{Eu}^{2+}$ (1–5 mol %) nanophosphor at $\lambda_{\text{exc}} = 380$ nm with 6 h sonication time and 22 kHz power. (Inset excitation spectrum of $\text{Sr}_2\text{SiO}_4: \text{Eu}^{3+}$ (2 mol %) nanophosphor at $\lambda_{\text{emi}} = 648$ nm.) (B) De-convoluted graph of PL emission spectra which supports for the Eu^{2+} transitions in the silicate host.

Fig.16. PL emission spectra of $\text{Sr}_2\text{SiO}_4:\text{Eu}^{3+}$ (1–5 mol %) nanophosphor at $\lambda_{\text{exc}}= 392$ nm with 6 h sonication time and 22 kHz power. (Inset excitation spectrum of $\text{Sr}_2\text{SiO}_4:\text{Eu}^{3+}$ (2 mol %) nanophosphor at $\lambda_{\text{emi}}= 613$ nm).

Fig.17. Energy levels diagram of Eu^{3+} and Eu^{2+} doped Sr_2SiO_4 nanophosphor.

Fig.18. Variation of asymmetric ratio in $\text{Sr}_2\text{SiO}_4:\text{Eu}^{3+}$ (1 – 5 mol %) nanophosphors.

Fig.19. Effect of concentration of Eu^{3+} and Eu^{2+} on maximum peak emission in Sr_2SiO_4 nanophosphors.

Fig.20. PL excitation spectrum, with the enlarge portion, showing the phonon assisted transition.

Fig.21. The schematic representation of concentration quenching in $\text{Sr}_2\text{SiO}_4:\text{Eu}^{3+}/\text{Eu}^{2+}$ nanophosphor.

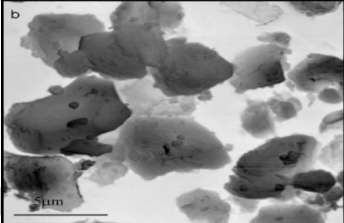
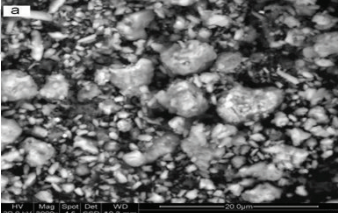
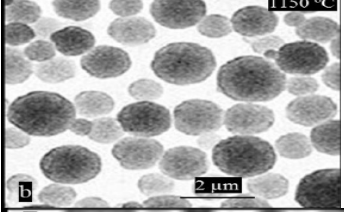
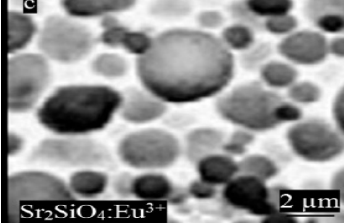
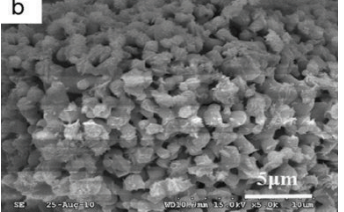
Fig.22. Relation between $\log(x)$ and $\log(I/x)$ in $\text{Sr}_2\text{SiO}_4:\text{Eu}^{3+/2+}$ (1 – 5mol %) nanophosphor.

Fig.23. CIE diagram of $\text{Sr}_2\text{SiO}_4:\text{Eu}^{3+}$ and Eu^{2+} (1 - 5 mol %) nanophosphor.

Fig.24. CCT diagram of $\text{Sr}_2\text{SiO}_4:\text{Eu}^{3+}$ and Eu^{2+} (1-5 mol %) nanophosphor.

Fig.25. Luminescence decay curves (A) $\text{Sr}_2\text{SiO}_4:\text{Eu}^{2+}$ (2 mol %) (B) $\text{Sr}_2\text{SiO}_4:\text{Eu}^{3+}$ (2 mol %) phosphors.

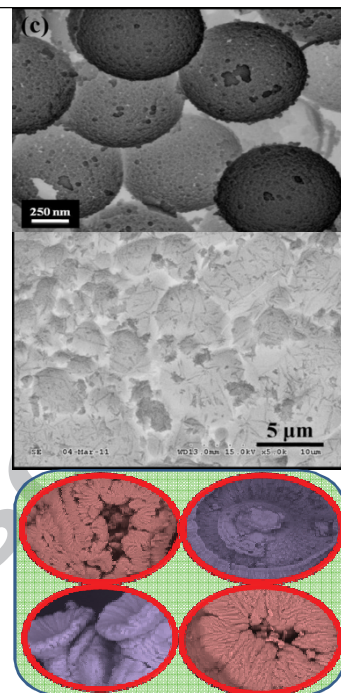
Table 1: List of $\text{Sr}_2\text{SiO}_4:\text{Eu}^{3+}$ synthesized by different methods, formation temperature and different morphologies of phosphor.

Method of synthesis	Formation temperature	Morphology	Ref.	SEM images
Solid-state reaction method	1300 °C for 3hrs	Small spherical particles	Zhengwei Pan, et.al. [10]	
Sol-gel route	600 °C for 2hrs	Small clusters with irregular shapes	S.K. Gupta, et.al. [11]	
Hybrid process	1300 °C for 3hrs	Needle-shaped particles	Jung Hye Park, et.al. [12]	
Spray-drying process	1150 °C for 5hrs	Spherical particles	Hao Feng, et.al. [13]	
Spray-drying process.	1200 °C for 5hrs	Spherical morphology	Fengjun Wei, et.al. [4]	
Microwave assisted method	1200 °C for 1hrs	Dumbbell shaped nanoparticles	Ru-Yuan Yang, et.al. [14]	

h-BN protective method 1200 °C for 8hrs Hollow spherical structure Jia-Ye Tang, et.al. [15]

Microwave assisted method 1200 °C for 2hrs spherical shape structure Huang-Yu Chen, et.al. [16]

Ultrasound method 600 °C for 3hrs SS Present work



ACCEPTED MANUSCRIPT

Table2: List of major phytochemicals extracted in *A.V.* gel confirmed from GCMS.

Name of the compound	Molecular Weight	Molecular formula
Tetracontane	562	C ₄₀ H ₈₂
Guanosine	283	C ₁₀ H ₁₃ N ₅ O ₅
Ethanone, 1-Phenyl	120	C ₈ H ₈ O
Pentadecanoic Acid	242	C ₁₅ H ₃₀ O ₂

Table 3: Estimated crystallite size, strain and energy gap (E_g) values of $\text{Sr}_2\text{SiO}_4:\text{Eu}^{3+}$ (1-5 mol %) nanophosphor.

Eu conc. (mol %)	Crystallite size(nm) [D-S approach]	Crystallite size(nm) [W-H approach]	Strain ($\times 10^{-4}$)	E_g(eV)
1	28.7	26.9	1.6	5.11
2	29.3	28.1	1.8	4.80
3	29.9	26.3	1.7	4.78
4	31.6	29.1	1.4	4.86
5	28.4	23.9	1.5	4.70

Table 4: Judd-Ofelt intensity parameters (Ω_2 , Ω_4), Emission peak wavelengths (λ_p in nm), radiative transition probability (A_T), calculated radiative (τ_{rad}) lifetime, branching ratio (β_R) and asymmetric ratio (A_{21}) of $Sr_2SiO_4:Eu^{3+}$ (1-5 mol %) compounds ($\lambda_{ex} = 392$ nm).

$Sr_2SiO_4:Eu^{3+}$ conc. (mol%)	Judd-Ofelt intensity parameters ($\times 10^{-20} \text{ cm}^2$)		Emission peak wavelength λ_p in nm	A_T (s^{-1})	τ_{rad} (ms)	β_R	A_{21}
	Ω_2	Ω_4					
1	5.91	3.78	612.91	133.09	7.51	0.999	16.41
2	6.60	3.88	612.91	148.55	6.73	0.997	15.32
3	6.87	3.49	612.91	154.79	6.46	0.999	10.98
4	6.15	3.91	612.80	138.56	7.21	0.990	10.49
5	6.41	3.49	612.91	144.33	6.92	0.998	10.87

Table.5. Photometric characteristics of Eu^{3+} and Eu^{2+} doped Sr_2SiO_4 nanophosphors.

Eu Concentration (mol %)	$\text{Sr}_2\text{SiO}_4: \text{Eu}^{3+}$				$\text{Sr}_2\text{SiO}_4: \text{Eu}^{2+}$			
	X	Y	CCT (K)	CP (%)	X	Y	CCT (K)	CP (%)
1	0.6053	0.3941	1309	92.1	0.3816	0.4669	4414	89
2	0.6181	0.3814	1018	93	0.3794	0.4617	4440	90
3	0.6170	0.3824	1047	92.4	0.3840	0.4716	4384	88.6
4	0.6185	0.381	1006	92.8	0.3882	0.4742	4313	89.4
5	0.6136	0.3858	1134	91.23	0.3642	0.4752	4794	88.5

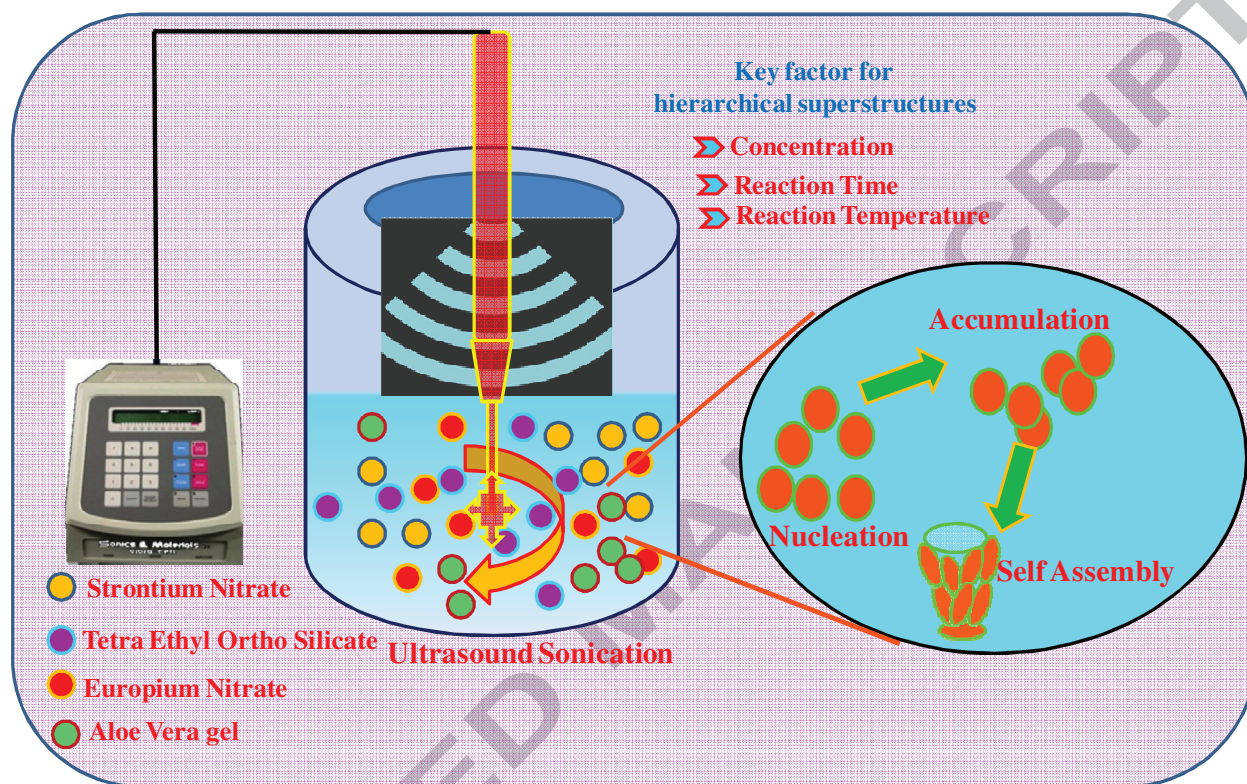


Fig.1. Schematic for the synthesis of Eu^{3+} doped Sr_2SiO_4 nanophosphor by ultrasonication method.

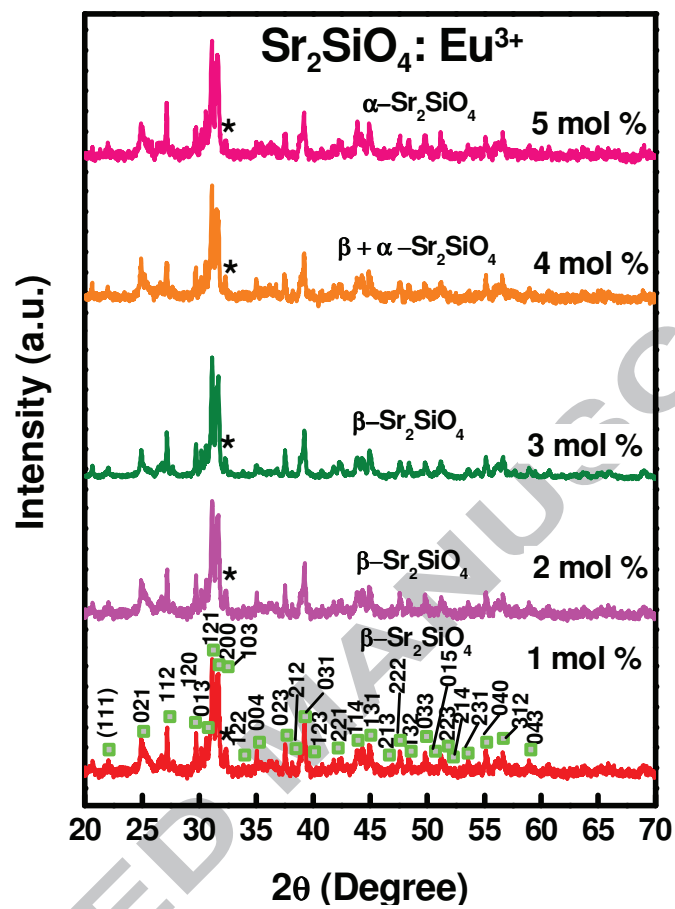


Fig.2 (a).PXRD patterns of Sr₂SiO₄: Eu³⁺ (1–5 mol %) nanophosphor.

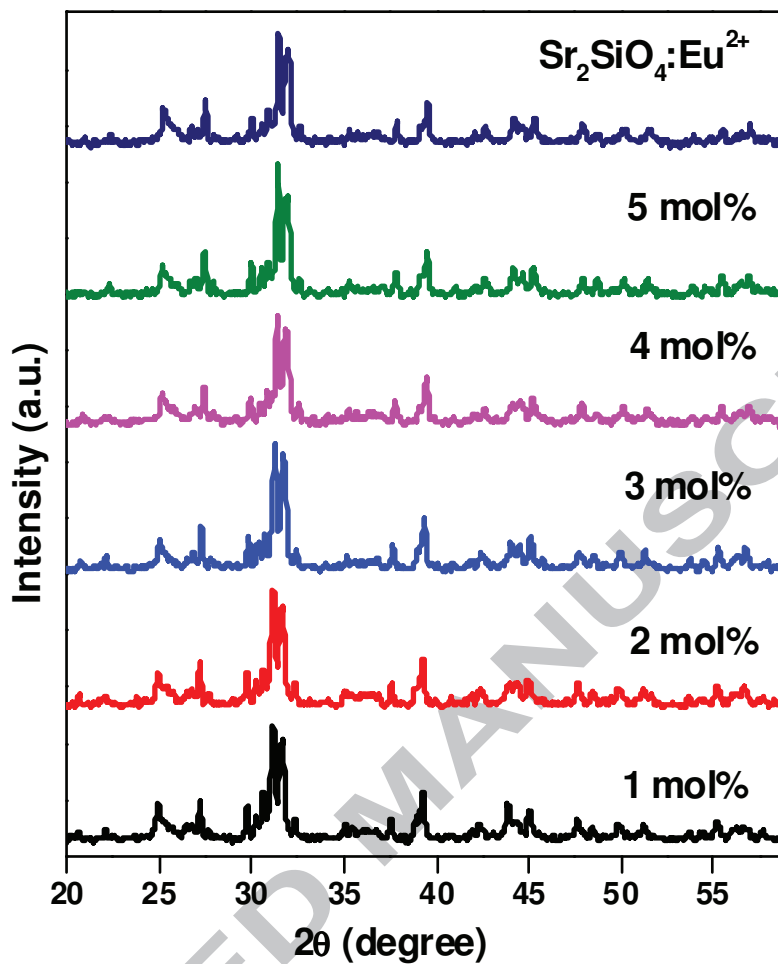


Fig.2 (b).PXRD patterns of $\text{Sr}_2\text{SiO}_4:\text{Eu}^{2+}$ (1–5 mol %) nanophosphor.

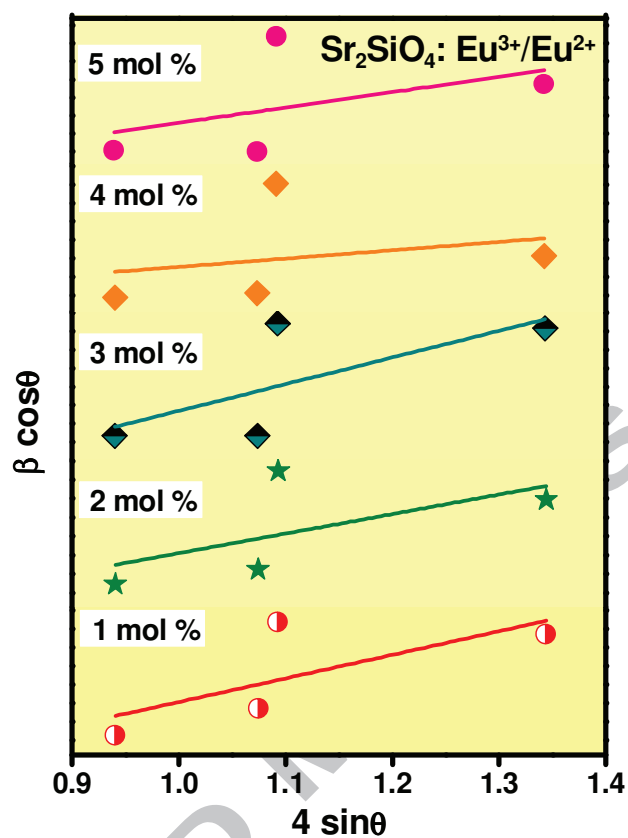


Fig.3. W-H plots of $\text{Sr}_2\text{SiO}_4: \text{Eu}^{3+}/\text{Eu}^{2+}$ (1–5 mol %) nanophosphor.

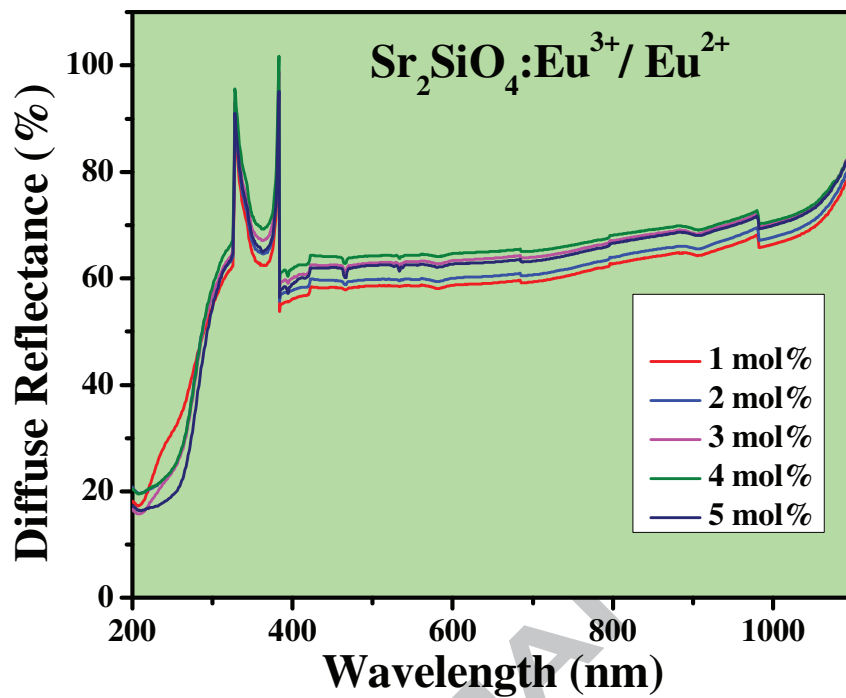


Fig.4. Diffuse reflectance spectra of $\text{Sr}_2\text{SiO}_4:\text{Eu}^{3+}/\text{Eu}^{2+}$ (1–5 mol %) nanophosphor.

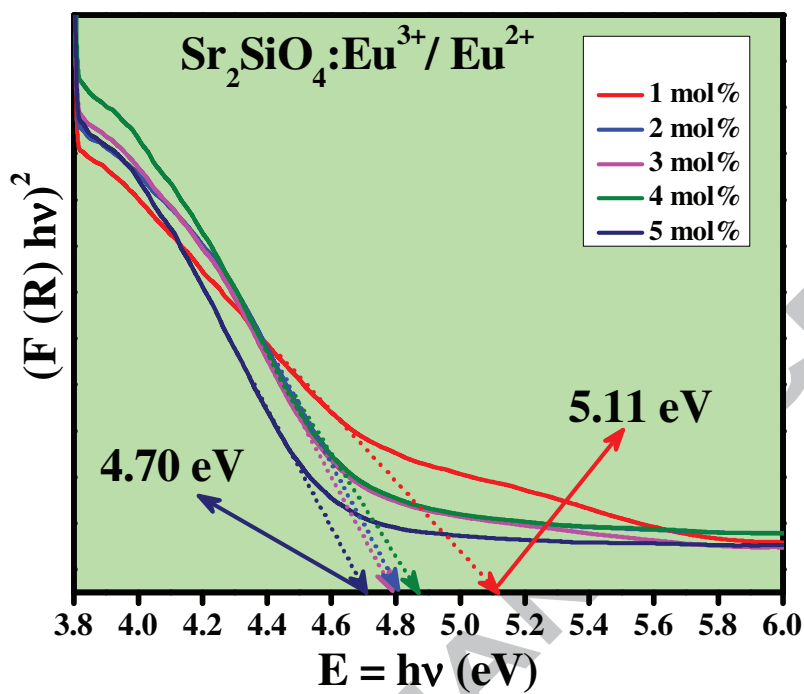


Fig.5. Energy band gaps of $\text{Sr}_2\text{SiO}_4:\text{Eu}^{3+}/\text{Eu}^{2+}$ (1–5 mol %) nanophosphor.

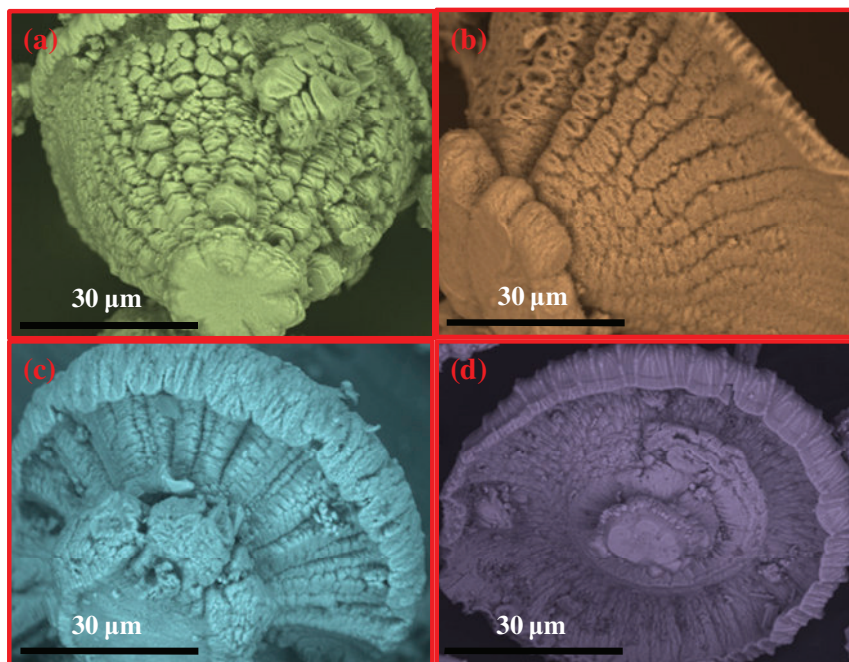


Fig.6. SEM images of Sr₂SiO₄: Eu³⁺ (2 mol %) nanophosphor with different sonication power (20, 22, 24 and 26 kHz).

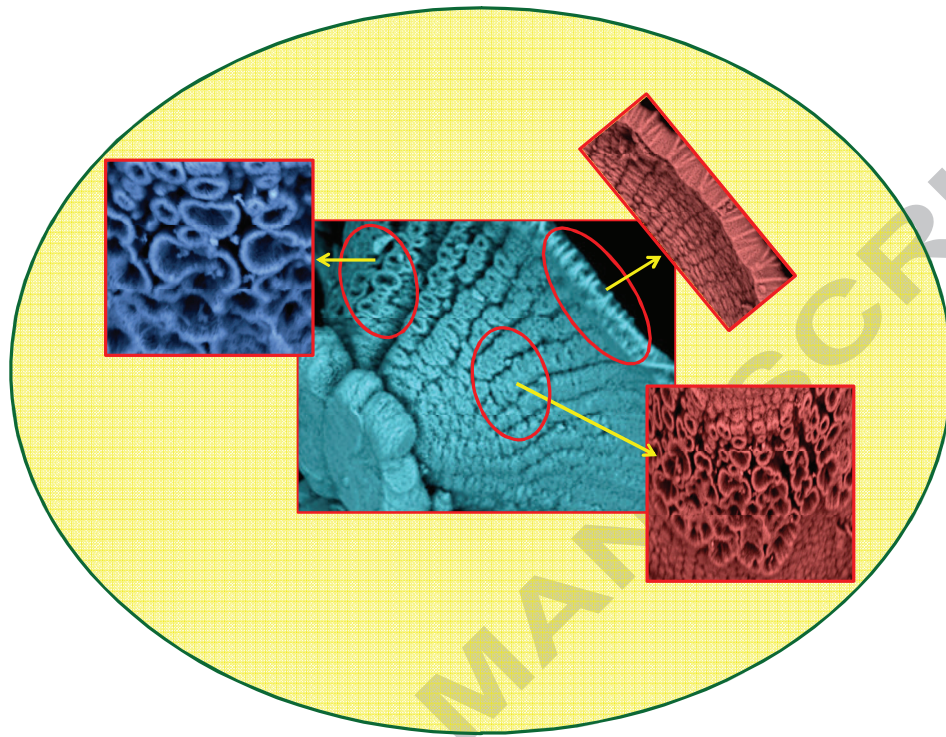


Fig.7. SEM images of Sr₂SiO₄: Eu³⁺ (2 mol %) nanophosphor with sonication power 22 kHz with its enlarged portions.

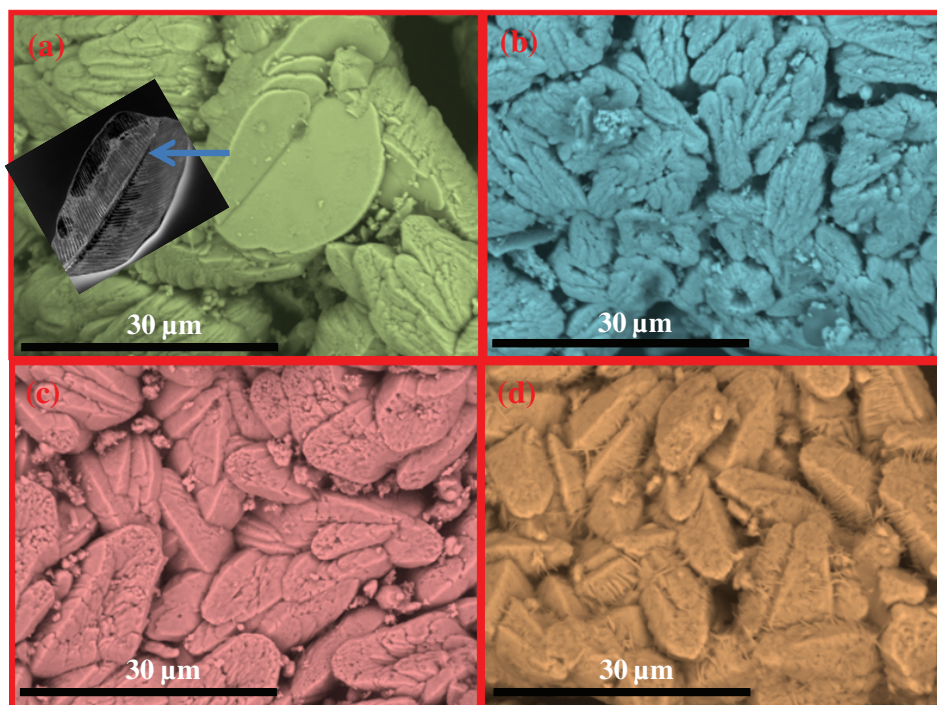


Fig.8. SEM images of $\text{Sr}_2\text{SiO}_4: \text{Eu}^{3+}$ (2 mol %) nanophosphor with different concentration of A.V. (5, 10, 15 and 20 ml) with 1hr of ultrasonic irradiation time.

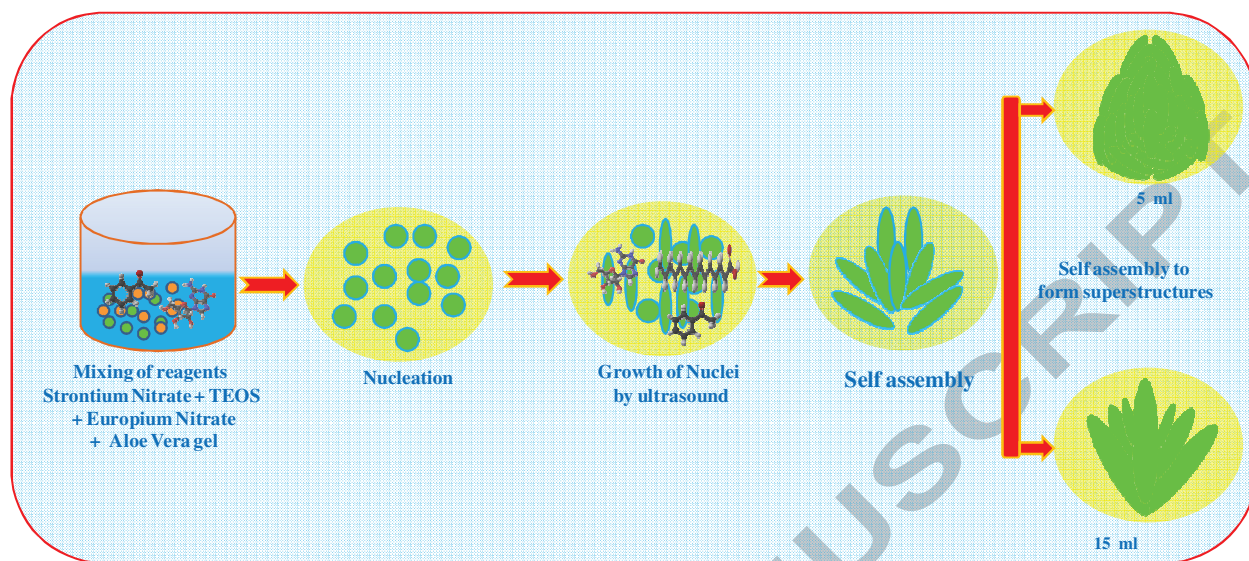


Fig.9. Schematic representation of formation process of SS in Sr₂SiO₄: Eu³⁺ (2 mol %) nanophosphor with different concentration of A. V..

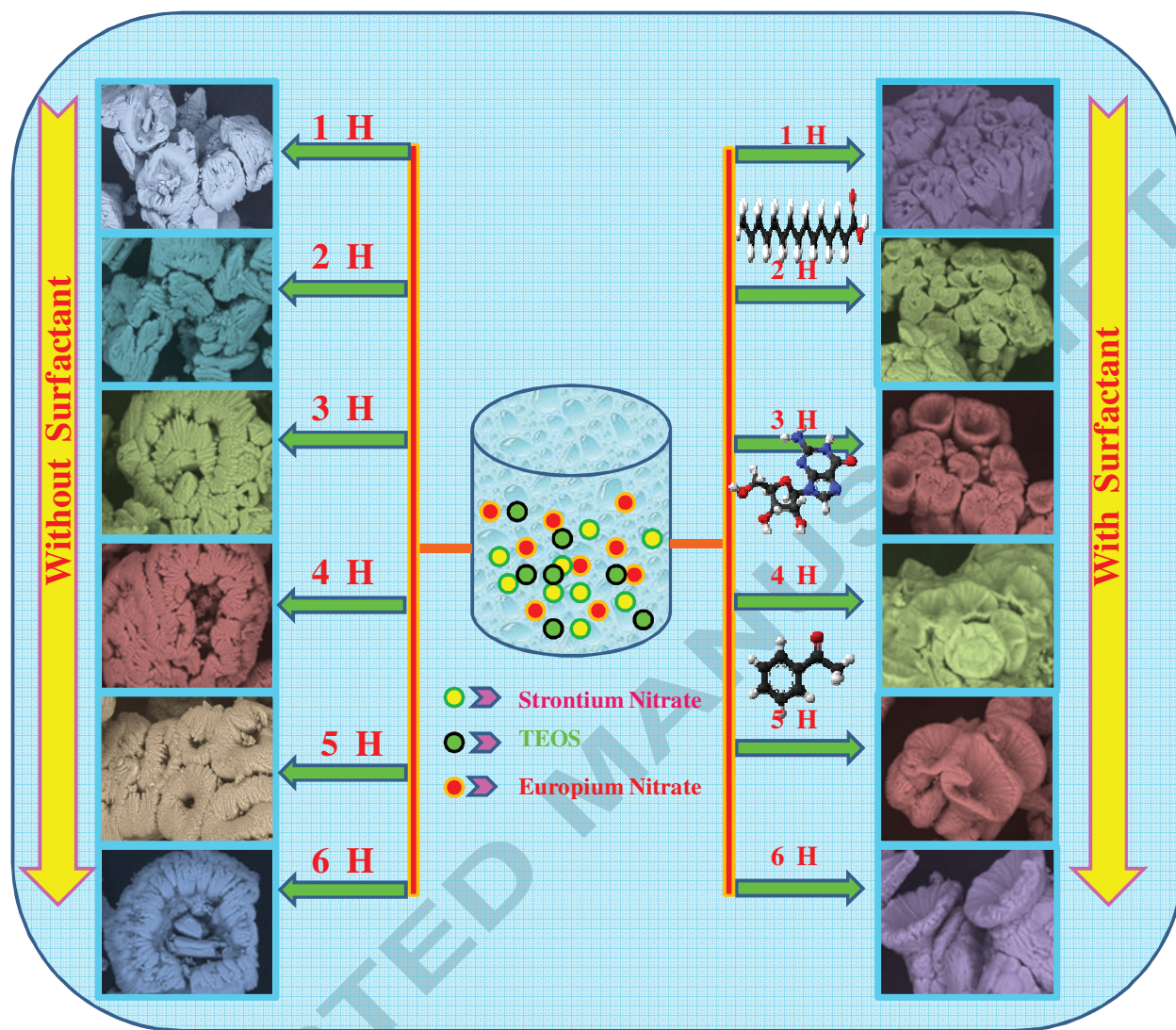


Fig.10. Schematic representation of formation process of different SS in Sr₂SiO₄: Eu³⁺ (2 mol %) nanophosphor.

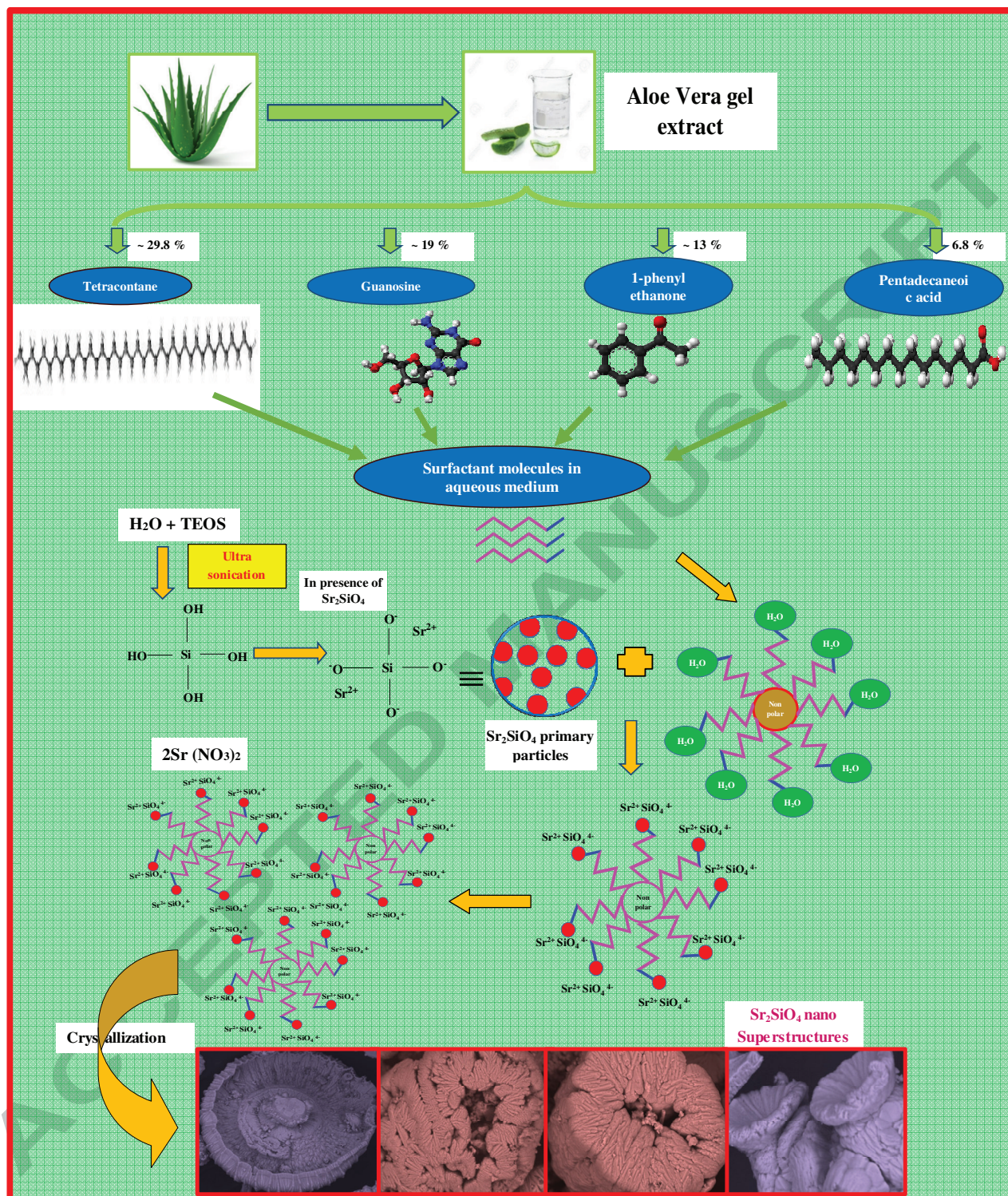


Fig.11. Schematic representation of $\text{Sr}_2\text{SiO}_4:\text{Eu}^{3+}$ nanostructures in the presence of A.V..

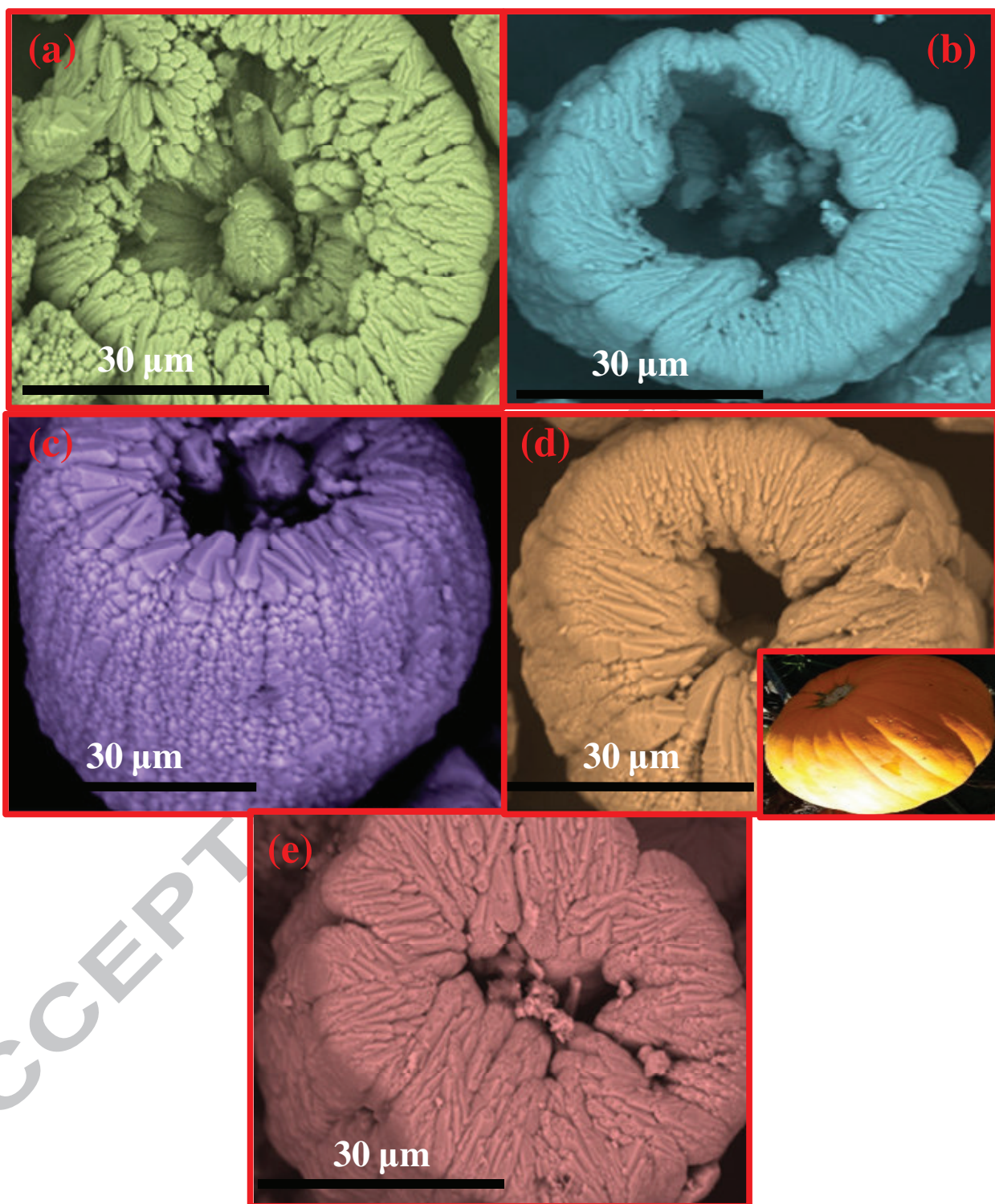


Fig.12.SEM images of $\text{Sr}_2\text{SiO}_4: \text{Eu}^{3+}$ (2 mol %) nanophosphor with various pH values (5, 7, 9, 11 and 12) with 1hr of ultrasonic irradiation time.

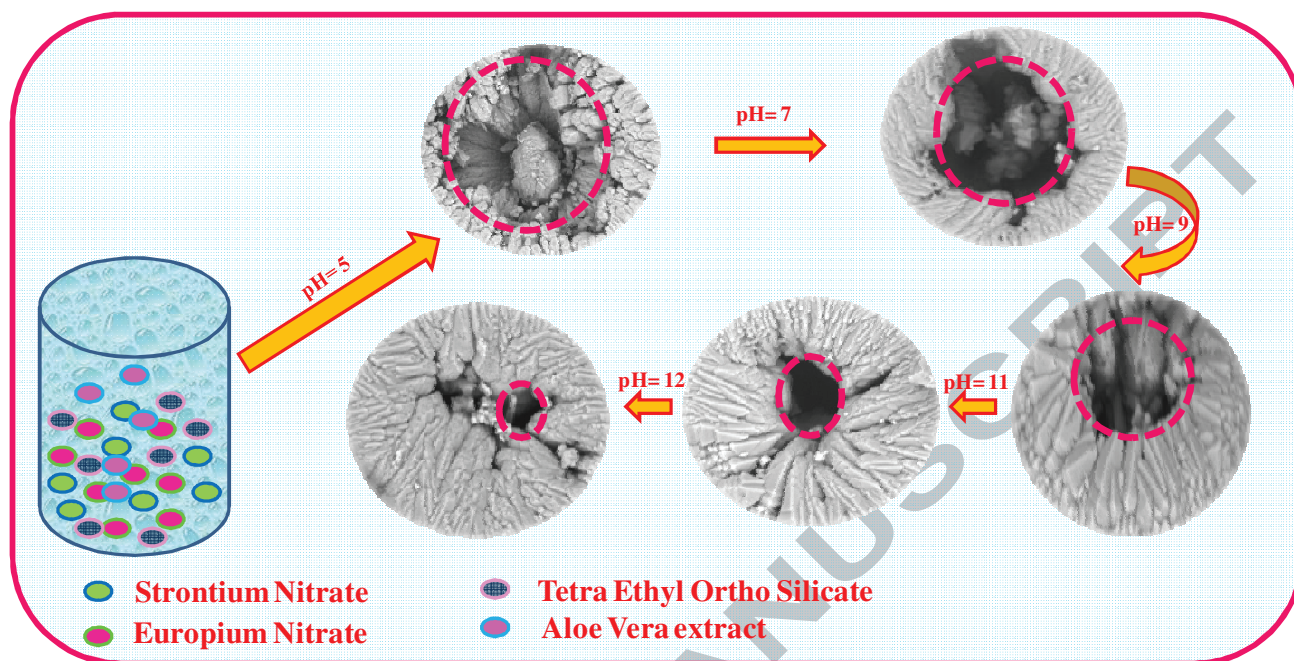


Fig.13.Schematic representation for the formation of hierarchical SS of $\text{Sr}_2\text{SiO}_4:\text{Eu}^{3+}$ (2 mol %) nanophosphor with various pH values.

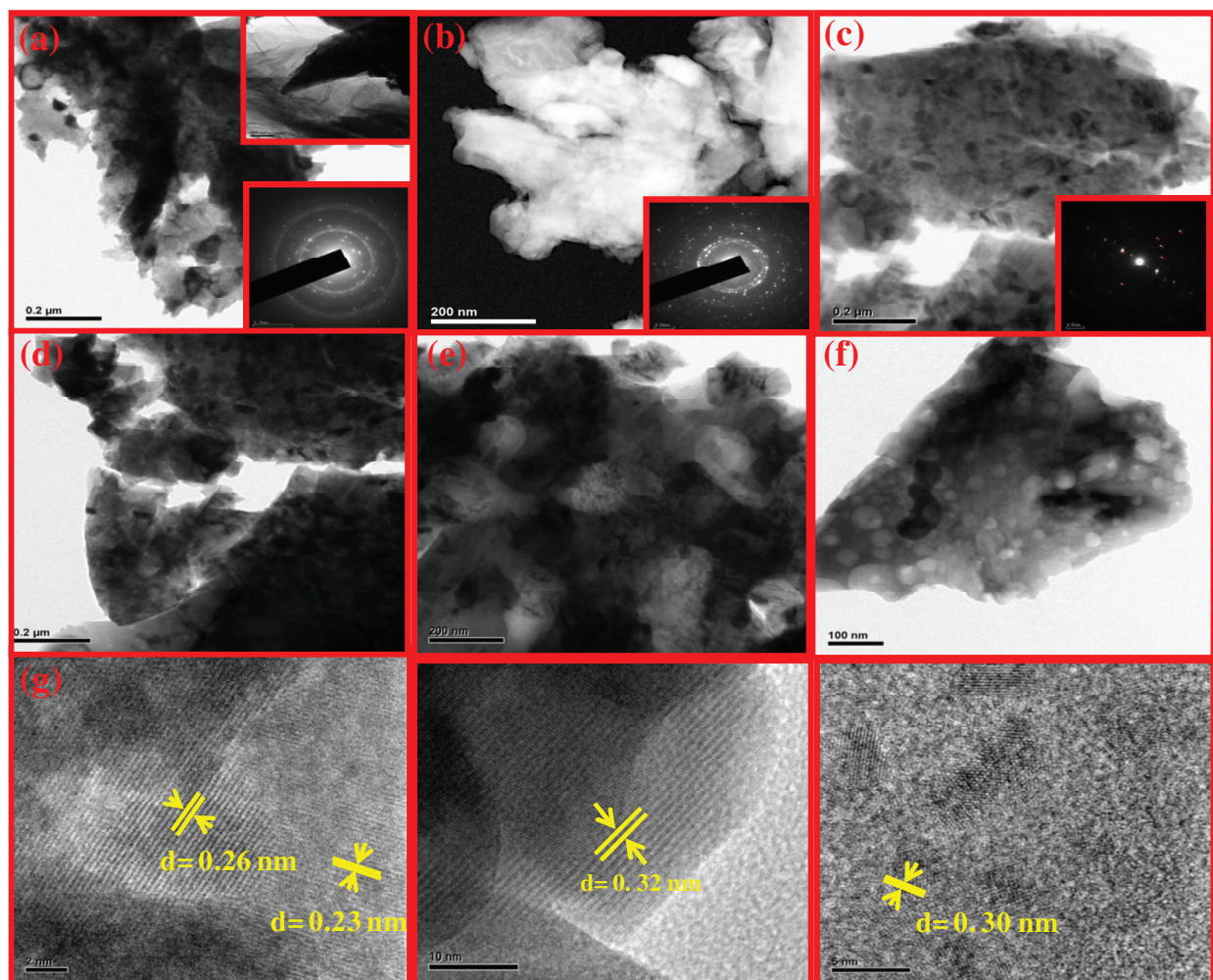


Fig. 14. TEM and HRTEM images of $\text{Sr}_2\text{SiO}_4: \text{Eu}^{3+}/\text{Eu}^{2+}$ (1, 3 & 5 mol %) nanophosphor with 1h sonication time.

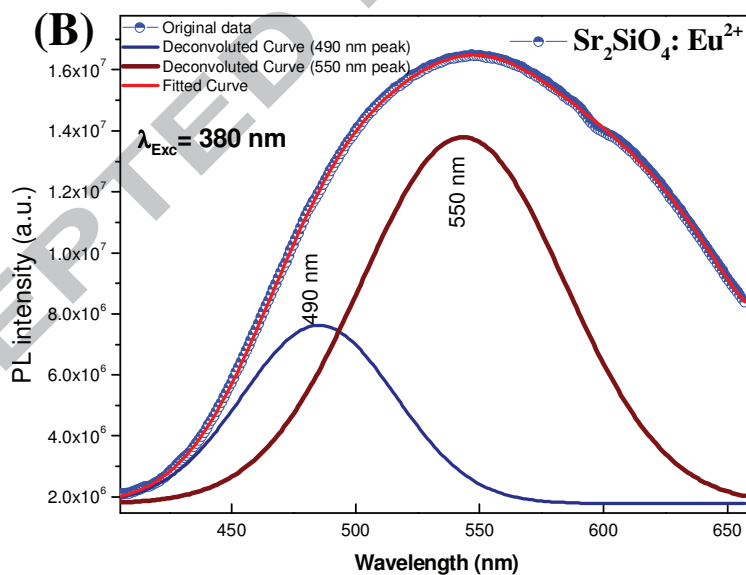
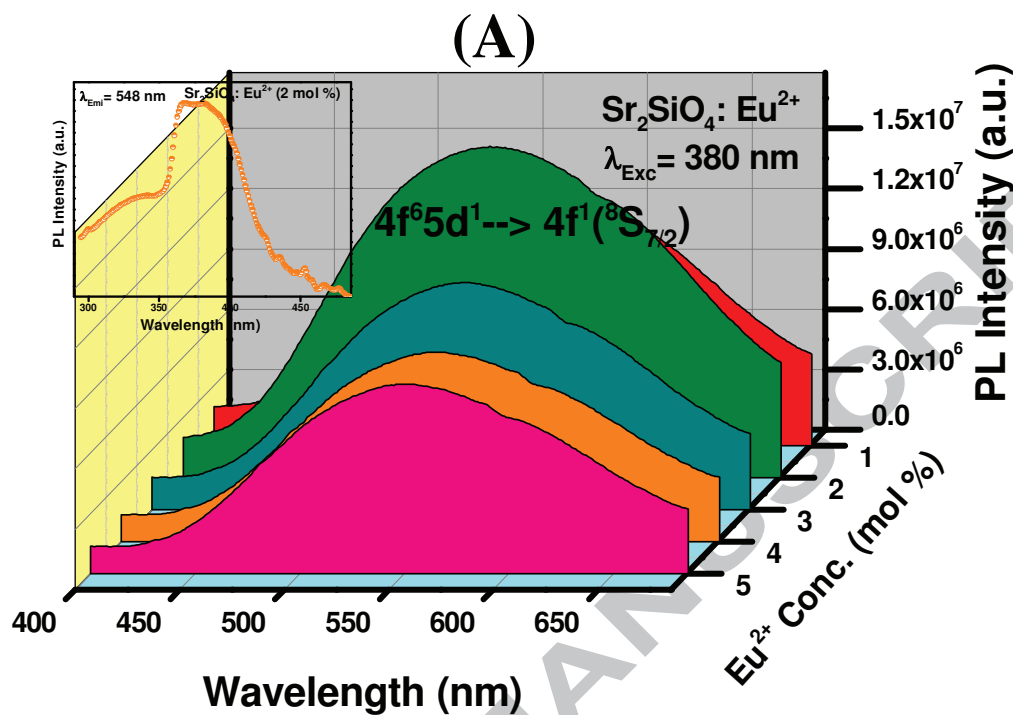


Fig.15. (A) PL emission spectra of $\text{Sr}_2\text{SiO}_4:\text{Eu}^{2+}$ (1–5 mol %) nanophosphor at $\lambda_{\text{exc}} = 380 \text{ nm}$ with 6 h sonication time and 22 kHz power. (Inset excitation spectrum of $\text{Sr}_2\text{SiO}_4:\text{Eu}^{2+}$ (2 mol %) nanophosphor at $\lambda_{\text{emi}} = 648 \text{ nm}$.) (B) Deconvoluted graph of PL emission spectra which supports for the Eu^{2+} transitions in the silicate host.

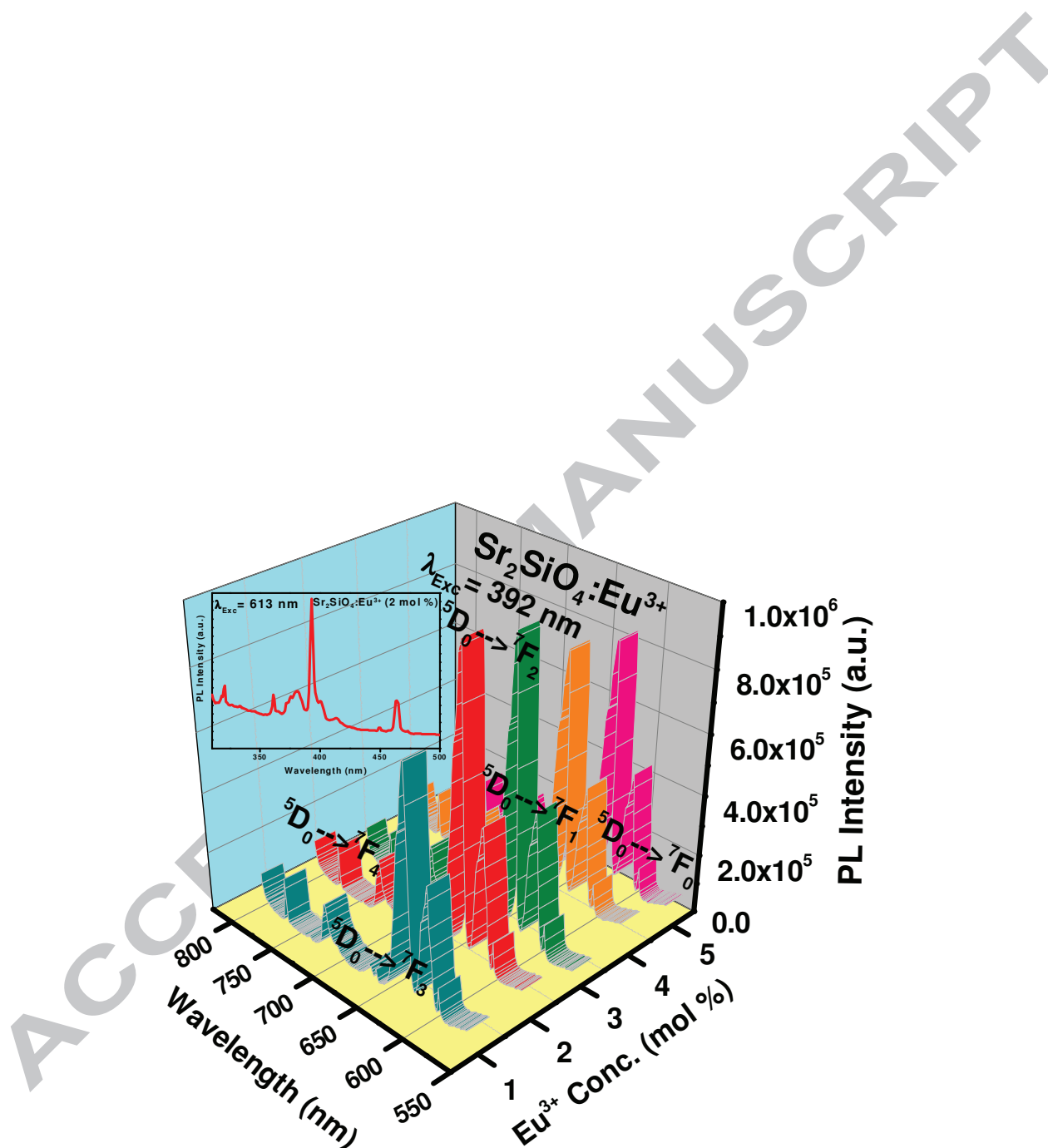


Fig.16. PL emission spectra of Sr₂SiO₄: Eu³⁺ (1–5 mol %) nanophosphor at λ_{exc}= 392 nm with 6 h sonication time and 22 kHz power. (Inset excitation spectrum of Sr₂SiO₄: Eu³⁺ (2 mol %) nanophosphor at λ_{emi}= 613 nm).

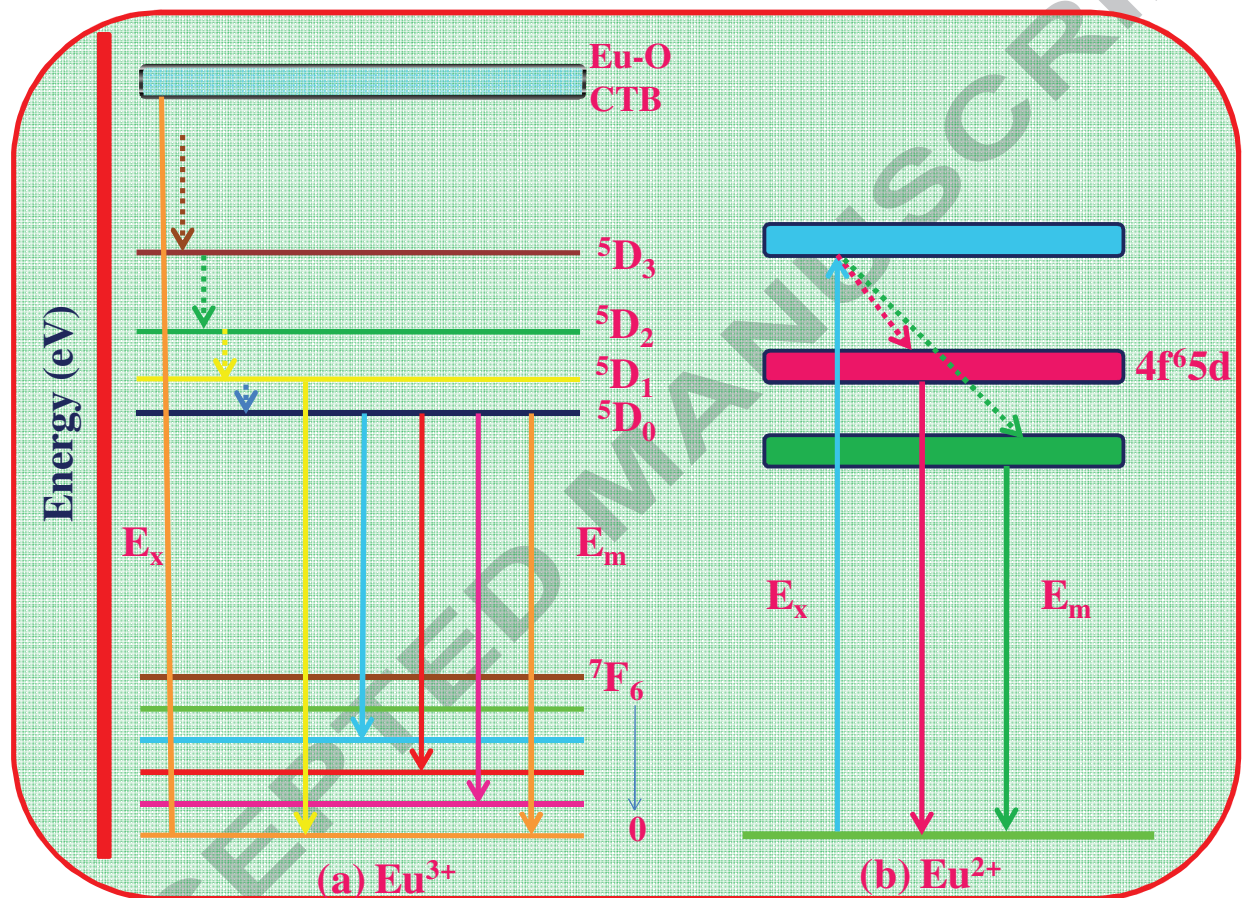


Fig.17. Energy levels diagram of Eu^{3+} and Eu^{2+} doped Sr_2SiO_4 nanophosphor.

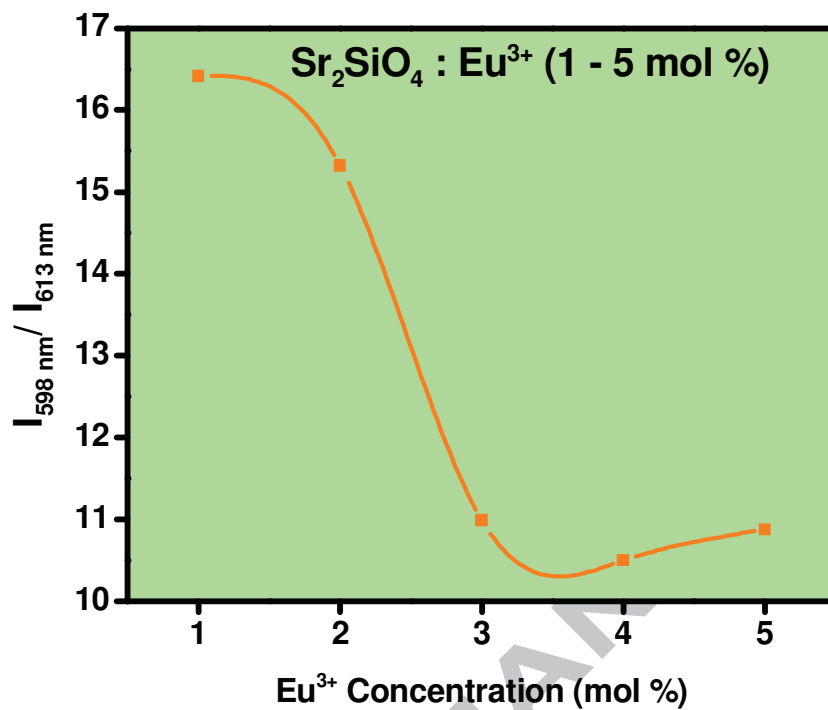


Fig.18. Variation of asymmetric ratio in $\text{Sr}_2\text{SiO}_4 : \text{Eu}^{3+}$ (1 – 5 mol %) nanophosphors.

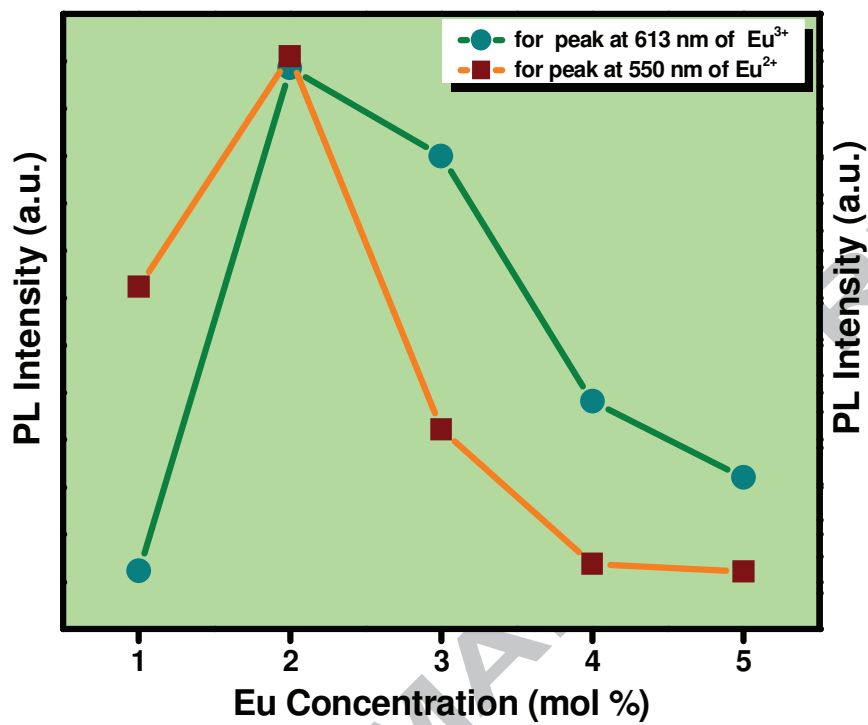


Fig.19. Effect of concentration of Eu^{3+} and Eu^{2+} on maximum peak emission in Sr_2SiO_4 nanophosphors.

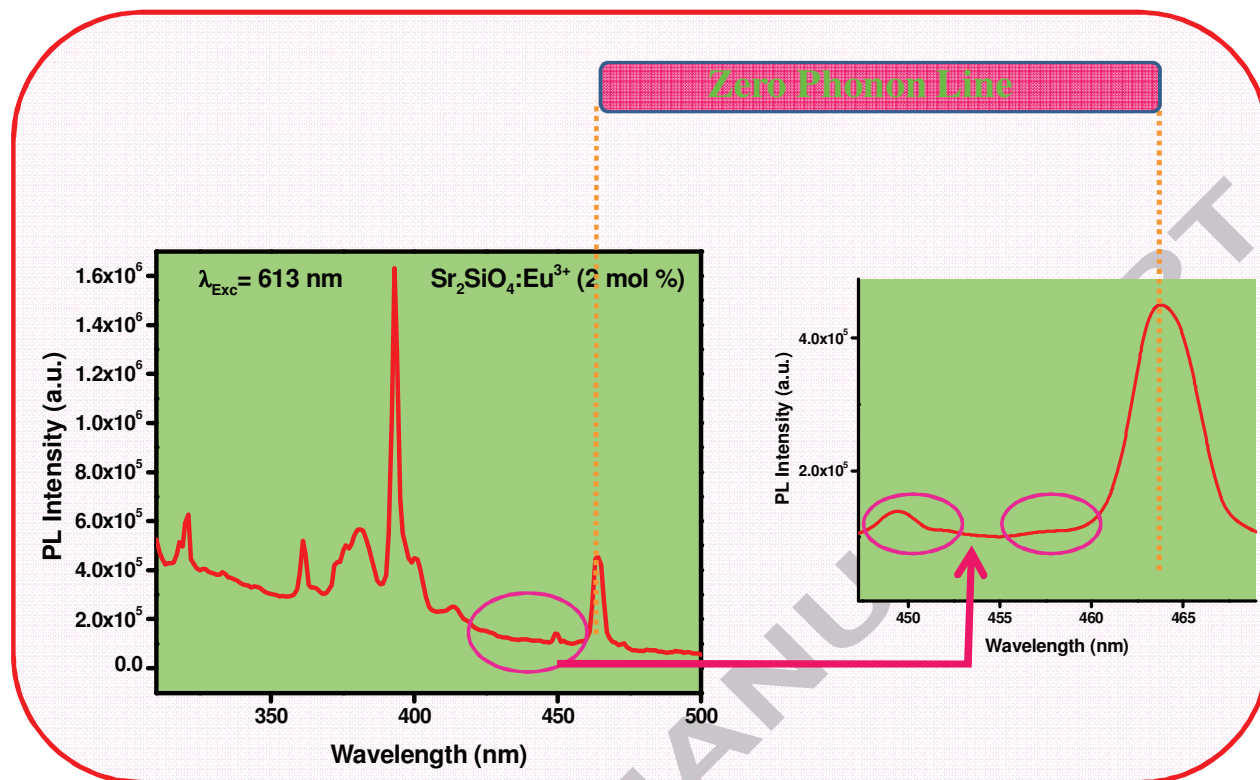


Fig.20. PL excitation spectrum, with the enlarge portion, showing the phonon assisted transition.

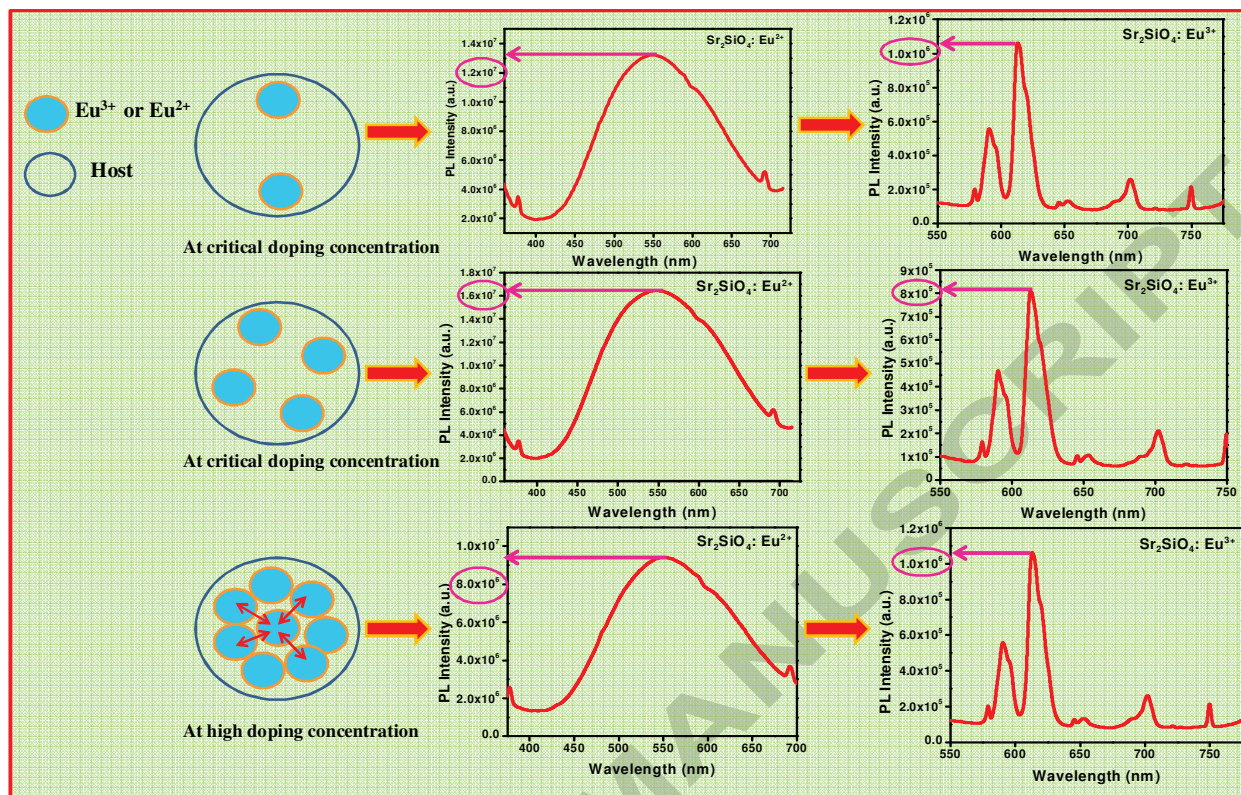


Fig.21. The schematic representation of concentration quenching in $\text{Sr}_2\text{SiO}_4: \text{Eu}^{3+}/\text{Eu}^{2+}$ nanophosphor.

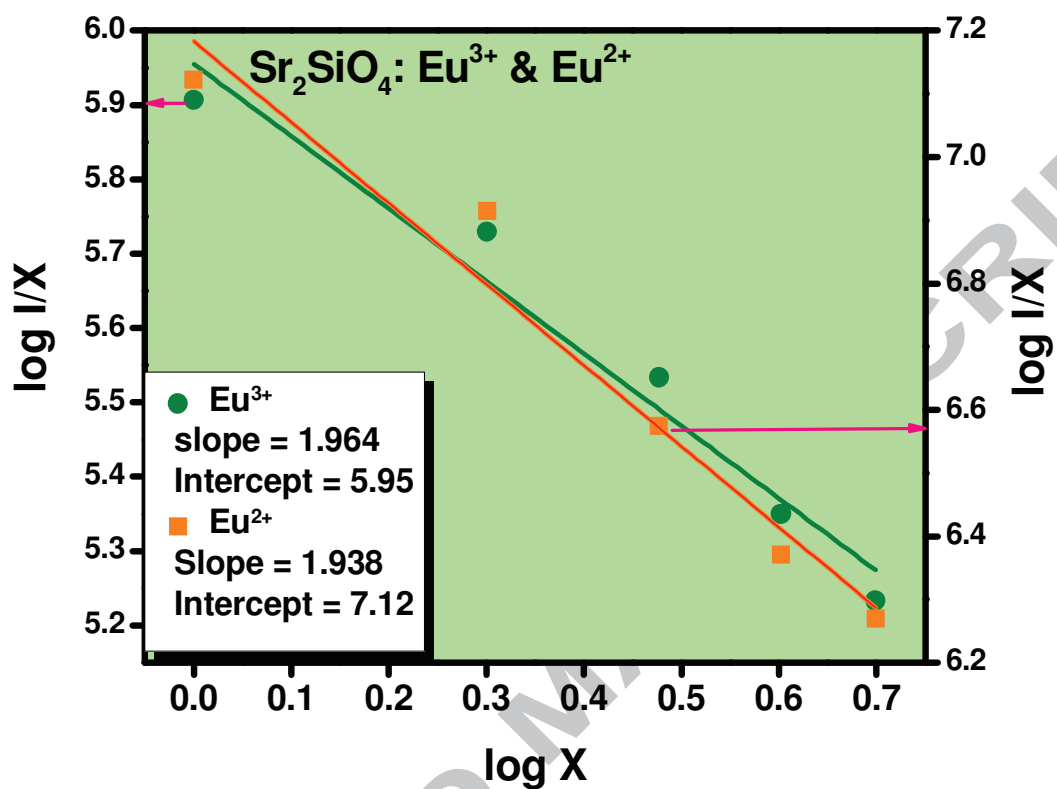


Fig.22. Relation between $\log(x)$ and $\log(I/x)$ in $\text{Sr}_2\text{SiO}_4: \text{Eu}^{3+/2+}$ (1 – 5mol %) nanophosphor.

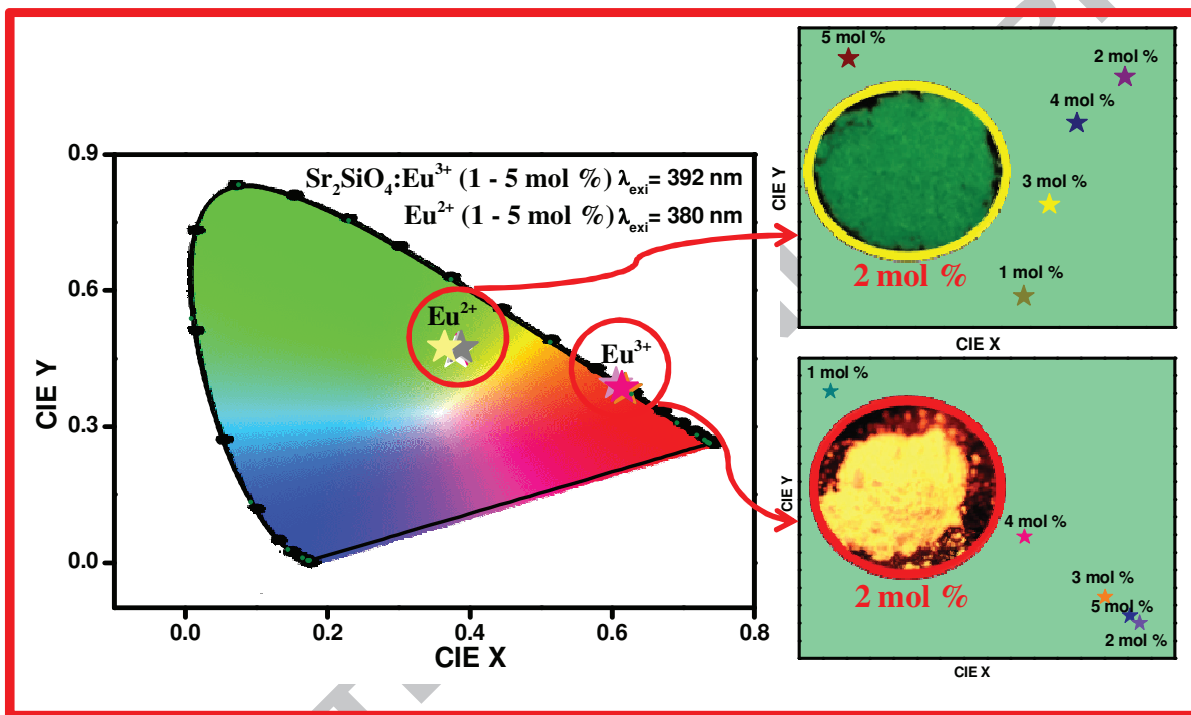


Fig.23. CIE diagram of $\text{Sr}_2\text{SiO}_4:\text{Eu}^{3+}$ and Eu^{2+} (1 - 5 mol %) nanophosphor.

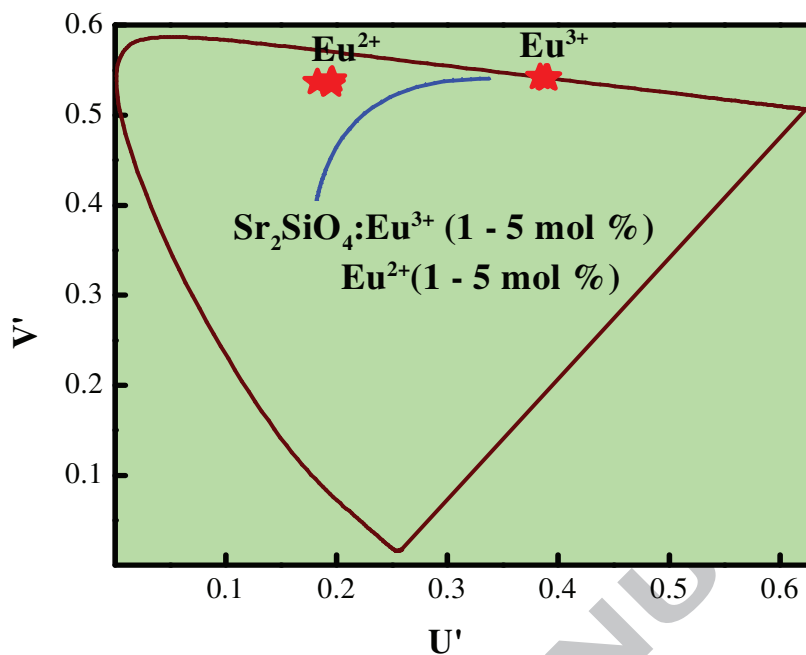


Fig.24. CCT diagram of $\text{Sr}_2\text{SiO}_4:\text{Eu}^{3+}$ and Eu^{2+} (1-5 mol %) nanoposphor.

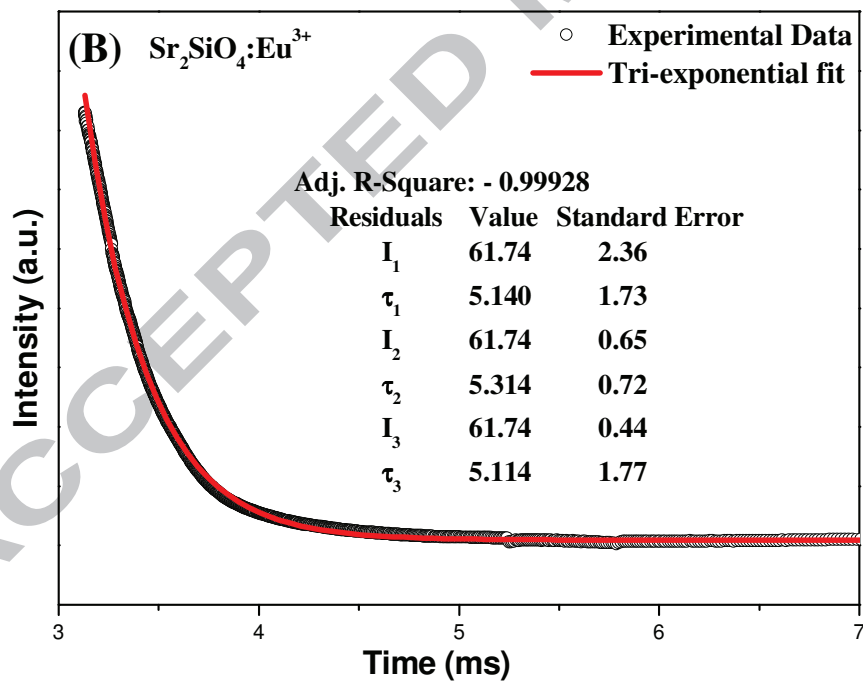
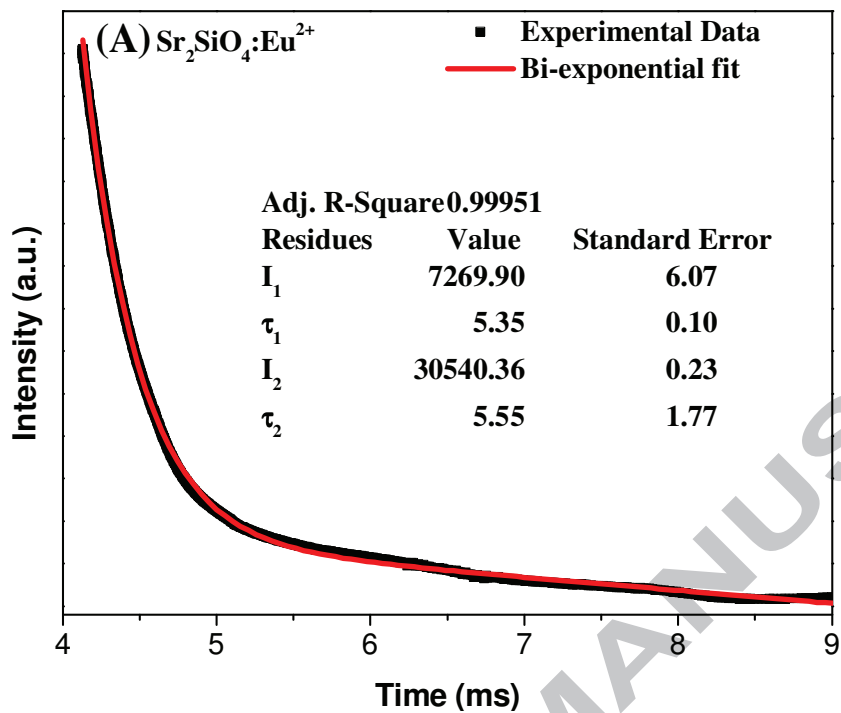
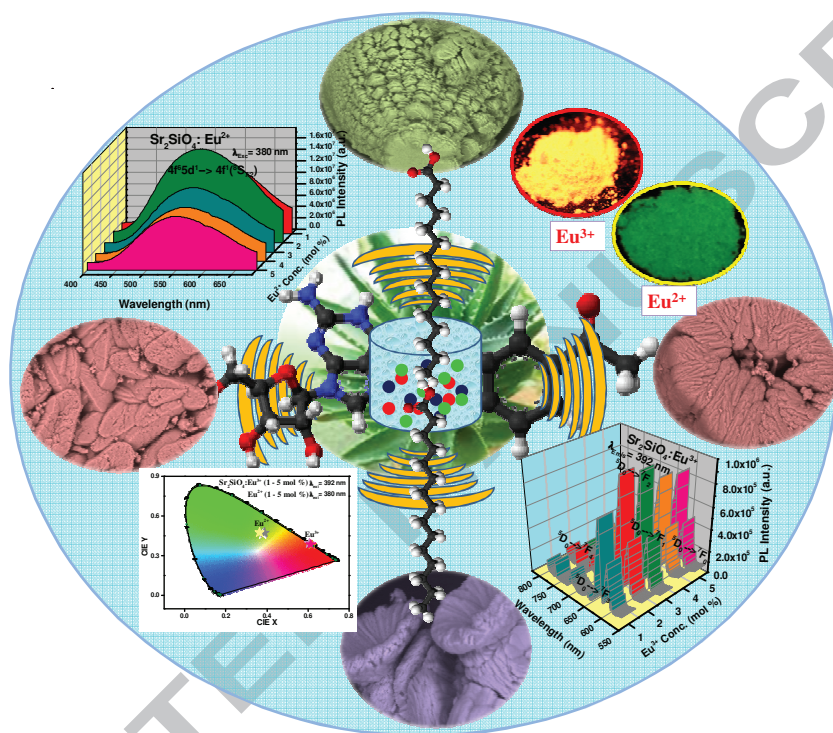


Fig. 25. Luminescence decay curves (A) $\text{Sr}_2\text{SiO}_4:\text{Eu}^{2+}$ (2 mol %) (B) $\text{Sr}_2\text{SiO}_4:\text{Eu}^{3+}$ (2 mol %) phosphors.

Graphical Abstract:



Research highlights:

- Superstructures of Sr_2SiO_4 : Eu was synthesized by ultrasound assisted combustion.
- The superstructures were analyzed systematically using PXRD, TEM, SEM, DRS etc.
- Possible mechanisms for the morphological superstructures were proposed.
- The obtained products were favorable for red and green component in white LEDs.